JGR Atmospheres

RESEARCH ARTICLE
10.1029/2023JD039310

Remote Sensing Measurements at a Rural Site in China: Implications for Satellite NO_2 and HCHO Measurement Uncertainty and Emissions From Fires

Kezhen Chong[1], Yuhang Wang[1], Cheng Liu[2], Yang Gao[3], K. Folkert Boersma[4], Jianhui Tang[5], and Xinming Wang[6]

[1]School of Earth and Atmospheric Sciences, Georgia Institute of Technology, Atlanta, GA, USA, [2]University of Science and Technology of China, Hefei, China, [3]Key Laboratory of Marine Environment and Ecology, Ministry of Education, Ocean University of China, Qingdao, China, [4]Satellite Observations Department, De Bilt, KNMI, Netherlands and Wageningen University, Wageningen, The Netherlands, [5]Yantai Institute of Coast Zone Research, CAS, Yantai, China, [6]Guangzhou Institute of Geochemistry, Chinese Academy of Sciences, Guangzhou, China

Key Points:

- Satellite NO_2 products are in much better agreement with MAX-DOAS measurements than HCHO products
- TROPOMI HCHO products have a significantly lower RMSE and better correlation with MAX-DOAS data than OMI HCHO products
- Agricultural burning can significantly enhance HONO, NO_2, and HCHO in the upper boundary layer, but enhancements due to fires, particularly of HONO, are highly variable

Supporting Information:

Supporting Information may be found in the online version of this article.

Correspondence to:

Y. Wang,
yuhang.wang@eas.gatech.edu

Citation:

Chong, K., Wang, Y., Liu, C., Gao, Y., Boersma, K. F., Tang, J., & Wang, X. (2024). Remote sensing measurements at a rural site in China: Implications for satellite NO_2 and HCHO measurement uncertainty and emissions from fires. *Journal of Geophysical Research: Atmospheres*, *129*, e2023JD039310. https://doi.org/10.1029/2023JD039310

Received 24 MAY 2023
Accepted 3 JAN 2024

Abstract Nitrogen dioxide (NO_2) and formaldehyde (HCHO) play vital roles in atmospheric photochemical processes. Their tropospheric vertical column density (TVCD) distributions have been monitored by satellite instruments. Evaluation of these observations is essential for applying these observations to study photochemistry. Assessing satellite products using observations at rural sites, where local emissions are minimal, is particularly useful due in part to the spatial homogeneity of trace gases. In this study, we evaluate OMI and TROPOMI NO_2 and HCHO TVCDs using multi-axis differential optical absorption spectroscopy (MAX-DOAS) measurements at a rural site in the east coast of the Shandong province, China in spring 2018 during the Ozone Photochemistry and Export from China Experiment (OPECE) measurement campaign. On days not affected by local burning, we found generally good agreement of NO_2 data after using consistent a priori profiles in satellite and MAX-DOAS retrievals and accounting for low biases in scattering weights in one of the OMI products. In comparison, satellite HCHO products exhibited weaker correlations with MAX-DOAS data, in contrast to satellite NO_2 products. However, TROPOMI HCHO products showed significantly better agreement with MAX-DOAS measurements compared to OMI data. Furthermore, case studies of the vertical profiles measured by MAX-DOAS on burning days revealed large enhancements of nitrous acid (HONO), NO_2, and HCHO in the upper boundary layer, accompanied with considerable variability, particularly in HONO enhancements.

Plain Language Summary We compared satellite NO_2 and HCHO tropospheric vertical columns (TVCDs), that is, the integrated column concentrations from the surface to the top of the troposphere, from OMI and TROPOMI instruments with ground-based MAX-DOAS measurements in spring 2018 at a rural coastal site in China. Our results on non-burning days indicate good agreement between satellite products and MAX-DOAS measurements for NO_2 TVCDs, albeit with some biases in one of the products. Potential factors contributing to the biases in that satellite product are investigated. Satellite HCHO products, however, did not compare as well with MAX-DOAS data as satellite NO_2 products, although TROPOMI HCHO products showed better agreement with MAX-DOAS data than OMI HCHO products. We further analyzed MAX-DOAS observations of HONO and HCHO on days with nearby agricultural burning activities. We found that HONO, NO_2, and HCHO can be significantly enhanced by burning, but the increase due to nearby fires, especially for HONO, is highly variable.

1. Introduction

Nitrogen dioxide (NO_2) and formaldehyde (HCHO) play critical roles in the tropospheric photochemical processes (Finlayson & Pitts, 1976; Levy et al., 2001; Lippmann, 1989; Nuvolone et al., 2018). NO_2 is an essential precursor for ozone (O_3) production in the troposphere and has both natural and anthropogenic sources (Felix & Elliott, 2014; Logan, 1983; Qu et al., 2020; Y. Wang et al., 1998). HCHO is produced during the oxidation of volatile organic compounds (VOCs), contributing to the productions of O_3 and aerosols. In the remote atmosphere, HCHO is mainly produced from methane (CH_4) oxidation. Over the continents, it is mainly produced by the oxidation of non-methane volatile organic compounds (NMVOCs) emitted from biogenic and anthropogenic

sources. Consequently, these emissions can be detected through the enhancements of short-lived HCHO (Dovrou et al., 2022; Z. Liu et al., 2012; Qu et al., 2021; Shim et al., 2005).

Observations of these trace gases provide valuable information to understand photochemical processes. Compared with surface measurements, which are limited in spatiotemporal coverages, satellite observations of tropospheric vertical column densities (TVCDs) can provide continuous data sets with a broad spatial range. The Ozone Monitoring Instrument (OMI) and the TROPOspheric Monitoring Instrument (TROPOMI) have provided continuous measurements of NO_2 and HCHO to advance our understanding of the related atmospheric chemical processes (Balamurugan et al., 2021; Lamsal et al., 2010; D. Li et al., 2021; J. Li & Wang, 2019; H. J. R. Wang et al., 2020; Zeng et al., 2008; Y. Zhang et al., 2018). OMI aboard NASA's Aura satellite has been in orbit since 2004. It has a local overpass time of around 13:45 local time (LT) and a nadir resolution of 13×24 km^2 (Levelt et al., 2006). TROPOMI onboard the European Copernicus Sentinel-5 Precursor (S5P) satellite was launched in 2017 and has extended the historical time series of midday observations from OMI with a local overpass time around 13:30 and an improved spatial resolution of 7×3.5 km^2 (5.5×3.5 km^2 after August 2019) (Veefkind et al., 2012). Both OMI and TROPOMI measure the backscattered radiance and solar irradiance in the visible and ultraviolet bands. The spectral windows of 328.5–359/356.5 nm and 402/405–465 nm are typically used to retrieve HCHO and NO_2 TVCDs, respectively (Krotkov et al., 2019a, 2019b; Smedt et al., 2017).

The increasing capability of satellite monitoring from space has enabled studies to better characterize pollution patterns, such as analyzing the responses of trace gases to either anthropogenic or biogenic sources (Balamurugan et al., 2021; Pu et al., 2022; R. Zhang et al., 2020) and investigating regional emission trends (DiMaria et al., 2023; Krotkov et al., 2016; J. Li & Wang, 2019). The uncertainties of satellite products consist of both systematic and random components. In rural regions, where TVCDs are usually low, satellite observations are subject to significant uncertainties that is, 45%–105% as reported in previous studies (González Abad et al., 2015, 2016). Validations of satellite observations are of particular interest to understanding sources of errors and improving retrieval accuracies (Boersma et al., 2004; J. T. Lin et al., 2014; Souri et al., 2022; P. Wang et al., 2022).

The multi-axis differential optical absorption spectroscopy (MAX-DOAS) instrument has been developed (Frieß et al., 2016; Hönninger et al., 2004) to simultaneously measure column densities of trace gases, including NO_2 and HCHO. Observing at multiple elevation angles, it can provide enhanced signals for low elevations with a horizontal spatial representativeness of the same order or even finer than the spatial resolution of satellite observations (Irie et al., 2011), thus has been utilized in assessments of satellite products. Such studies can be validations of a single satellite product (De Smedt et al., 2021; Ma et al., 2013; Verhoelst et al., 2021; Y. Wang et al., 2020; Xia et al., 2021; C. Zhang et al., 2020) or intercomparisons of several satellite products (De Smedt et al., 2021; Ialongo et al., 2016; Jin et al., 2016).

In addition to satellite validations, the simultaneous multicomponent observations from MAX-DOAS provide valuable vertical observational constraints of pollutants. These synchronous measurements have been utilized to analyze the fast-changing evolutions of complex photochemical processes, especially in relation to the impacts of biomass burnings (BB) on trace gases and aerosols. For instance, researchers have employed MAX-DOAS measured HCHO as a tracer for absorption aerosols to investigate brown carbon emissions from BB plumes at different stages (Irie et al., 2019). Other MAX-DOAS studies have focused on examining photochemical processes, such as ozone formation sensitivities (H. Lin et al., 2022) and the production mechanisms of nitrous acid (HONO), which has gained significant attention in recent years due to its potentially large impact on hydroxyl (OH) radicals (Hendrick et al., 2014; C. Liu et al., 2021).

In this study, we analyze MAX-DOAS observation at a rural coastal site in the Shandong province, China. On days when local fire emissions are minimal, we use these observations to evaluate different satellite products for NO_2 and HCHO TVCDs from OMI and TROPOMI. On days with active burning, we investigate the enhancements HONO, NO_2, and HCHO due to nearby agricultural burnings using MAX-DOAS observed vertical profiles of trace gases and aerosol extinction. We first provide descriptions of the satellite and MAX-DOAS observations in Section 2. We give an overview of intercomparison in Section 3.1, analyze the reasons for satellite differences in Section 3.2, investigate the HONO and HCHO enhancements from BB events in Section 3.3, and provide a summary in Section 4.

2. Materials and Methods

We obtained ground-based MAX-DOAS measurements from the Ozone Photochemistry and Export from China Experiment (OPECE) at a rural site located on the east coast of the Shandong province, between March 8 and

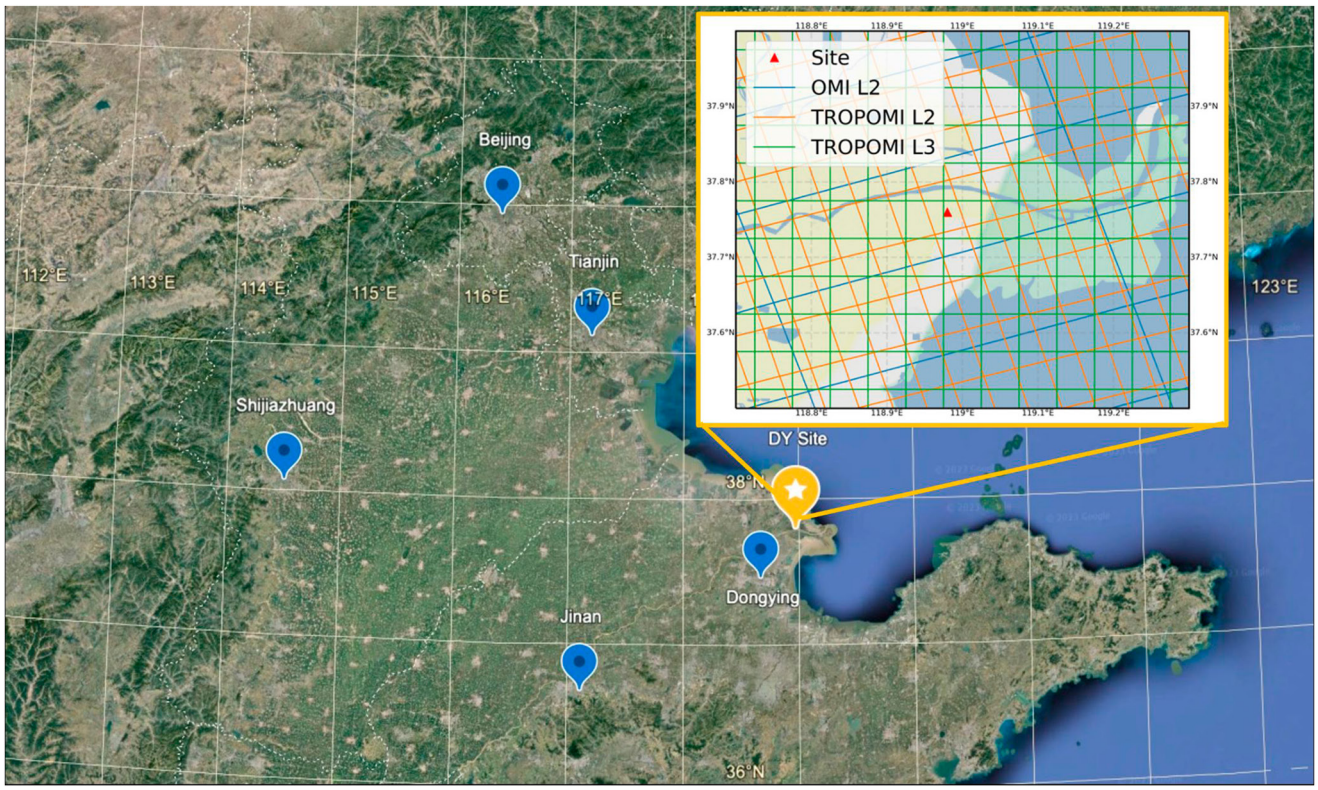

Figure 1. The observation site (yellow marker) and large cities (blue markers) (from Google Earth). The upper right panel shows the site location and satellite observation pixel grids for OMI L2, TROPOMI L2, and TROPOMI L3 products.

April 26, 2018. The site (37.76°N, 118.98°E) is 200–300 km downwind from the heavily polluted center of North China Plain (NCP), located at the estuary of the Yellow River near a national bird sanctuary (Figure 1). It is surrounded by crops and some off-line oil fields, and the city of Dongying, 50 km to the southwest of the site, is the only known area nearby with concentrated pollution emissions (Lee et al., 2021). The expansive flat terrain encompassing the site provides an optimal setting for remote sensing measurements.

Vertical profiles of NO_2, HCHO, HONO, sulfur dioxide (SO_2), and aerosol extinction coefficients (AEC) are obtained to evaluate satellite products on non-burning days and analyze agricultural burning impacts on burning days using a commercial MAX-DOAS instrument (Javed et al., 2020, 2021). The instrument has a spectral range between 300–460 nm with a spectral resolution of ~0.6 nm full width at half maximum (FWHM) (Hendrick et al., 2014; Y. Wang et al., 2018). Spectral observations were conducted at various elevation viewing angles controlled by a built-in mechanical processor. Detailed information about the instrumental operations can be found in previous works (Xing et al., 2017; Zheng et al., 2022). Differential slant column densities computed from the observed spectra by the QDOAS software (Danckaert et al., 2012) were combined with the differential air mass factors to derive the vertical column densities (VCDs). Trace gas profiles were retrieved based on the optimal estimation method (Rodgers, 2000) using a forward radiative transfer model (Frieß et al., 2016; Xing et al., 2017; Zheng et al., 2022). In this study, data measured with a solar zenith angle >75°, or DOAS fitting results with root mean square of residuals larger than 10^{-3} were filtered out.

Compared to surface and satellite observations, the MAX-DOAS instrument offers the advantage of measuring the vertical distribution of the boundary and upper layers. The average errors for near-surface (0–100 m) concentrations of NO_2, HCHO, HONO, and SO_2 were 0.1, 0.04, 0.14, and 0.16 parts per billion by volume (ppbV), respectively, and 0.11 for AEC, consistent with previous studies (Hendrick et al., 2014; Song et al., 2023). The MAX-DOAS data extends from the surface to 3 km (2.6 km for HONO and SO_2) at a 15-min time step and a vertical resolution of around 100 m below 2 km and 200 m above. Additionally, corresponding averaging kernels (AVKs) for each species are provided (Figure S1 in Supporting Information S1), which indicate good sensitivities of MAX-DOAS measurements within the boundary layer.

Table 1
Satellite Products and Their Abbreviations Used in This Work

Species	Data product	Abbreviations
NO_2	OMNO2 v4.0	OMI-NASA, NASA_REAM
NO_2	QA4ECV NO_2 v1.0	OMI-KNMI, KNMI_REAM
NO_2	TROPOMI v1.0.1	TROPOMI, TROPOMI_REAM
HCHO	OMHCHO v3	OMI-NASA, NASA_REAM
HCHO	QA4ECV HCHO v1.2	OMI-BIRA, BIRA_REAM
HCHO	TROPOMI L3	TROPOMI

In this study, we utilized six satellite products in total, and for simplicity purposes, we listed their abbreviations in Table 1. We obtained three Level-2 (L2) NO_2 TVCD products, including two OMI products: OMNO2 v4.0 from NASA (Krotkov et al., 2019a, 2019b) and QA4ECV NO_2 v1.0 from KNMI (Boersma et al., 2011), as well as the TROPOMI v1.0.1 operational product (van Geffen et al., 2021). We note that significant advancements in TROPOMI NO_2 products have been made since the v1.0.1 version. However, the newer TROPOMI product is unavailable for our study period (March–April 2018), which was during the commissioning phase of TROPOMI. We implemented cloud corrections to correct the bias in the TROPOMI v1 products.

The retrieval process for NO_2 TVCDs involves three steps: (a) fitting the slant column densities (SCDs) from the measured spectrum data using the differential optical absorption spectroscopy (DOAS) spectral fitting method (Platt & Stutz, 2008), (b) separating tropospheric SCDs (TSCDs) from the stratospheric SCDs, and (c) computing the tropospheric air mass factors (AMFs) based on scattering weights and a priori NO_2 profiles. The TVCDs are then obtained by dividing TSCDs by the AMFs (Bucsela et al., 2013; Eskes & Boersma, 2003; Platt & Stutz, 2008). The NASA and KNMI OMI NO_2 products differ in the processes of spectral fitting, tropospheric-stratospheric separation, and AMF calculation (Boersma et al., 2011; Bucsela et al., 2013; Griffin et al., 2019; Krotkov et al., 2017). The retrieval uncertainties for NO_2 TVCDs are approximately 30% under clear sky conditions and can be even higher in cloudy conditions (Boersma et al., 2011; Lamsal et al., 2014; J. Li et al., 2021; Lorente et al., 2017).

For HCHO TVCDs, we utilized the QA4ECV HCHO v1.2 product by the European consortium (BIRA, IUP, MPIC, KNMI, WUR) (De Smedt et al., 2015, 2017) and OMHCHO v3 product from NASA (Chance, 2007). As the TROPOMI L2 HCHO product (De Smedt et al., 2018) is not available for our study period, we obtained $0.05° \times 0.05°$ L3 daily data processed by the BIRA team (De Smedt et al., 2021). The retrieval process for HCHO TVCDs consists of three steps, (a) fitting the SCDs from the ultraviolet (UV) part of the spectra, (b) converting the SCDs to TVCDs using air mass factors retrieved from a look-up table, and (c) performing a background correction to correct for global offset and other factors. Therefore, the retrieved HCHO TVCD can be expressed as follows:

$$N_v = \frac{N_s - N_{s0}}{M} + N_{v0} \quad (1)$$

where M is the air mass factor, N_s is the SCD, N_{s0} and N_{v0} are the reference sector correction terms. More details can be found in the algorithm papers (De Smedt et al., 2018). The uncertainties of satellite HCHO products are related to pollution conditions and can be greater than 45% (González Abad et al., 2016), partly due to the nature of stronger Rayleigh scattering in the UV band, which limits the sensitivity to HCHO, especially in the lower atmosphere (Boersma et al., 2016).

The extensive utilizations of OMI and TROPOMI products worldwide (Levelt et al., 2018; J. Li & Wang, 2019; J. Li et al., 2021; K. Li et al., 2020; Sekiya et al., 2022; Wang, Beirle, et al., 2017; R. Zhang et al., 2018; Zhao & Wang, 2009) highlight the importance to ensure reliable data quality and mitigate factors that could contribute to the deviations among different products in the intercomparisons. To ensure the quality of data used in our study, we followed the instructions in the corresponding README files (Boersma et al., 2017; Krotkov et al., 2019a, 2019b; Smedt et al., 2017; van Geffen et al., 2021) to filter out any invalid or failed retrievals for all the satellite products. Specific quality filters used in this study are listed in Table S1 in Supporting Information S1.

Furthermore, it is important to consider the variations introduced by the use of different a priori profiles in the retrievals of OMI and TROPOMI products (e.g., Compernolle et al., 2020; Gu et al., 2014; Su et al., 2020). NASA retrievals employ monthly mean NO_2 profiles from the Global Modeling Initiative (GMI) model at $1° \times 1.25°$, as well as the monthly mean HCHO profiles from the GEOS-Chem model at a resolution of $2° \times 2.5°$ (Douglass et al., 2004; Lamsal et al., 2021). On the other hand, TROPOMI and KNMI retrievals utilize daily NO_2 or HCHO profiles from the Tracer Model version 5 (TM5-MP) at $1° \times 1°$ resolution (Boersma et al., 2017; van Geffen et al., 2021; Williams et al., 2017). In this work, we employed consistent a priori profiles simulated by the Regional chEmical trAnsport Model (REAM) in satellite and MAX-DOAS retrievals to facilitate the intercomparisons. REAM has been widely applied in previous studies (J. Li & Wang, 2019; J. Li et al., 2021;

Qu et al., 2020). It is a regional chemistry transport model with boundary conditions obtained from a 2° × 2.5° simulation from the GEOS-Chem model. REAM has a horizontal resolution of 36 km and 30 vertical layers in the troposphere, driven by meteorology fields from the Weather Research and Forecasting (WRF) model. The chemistry mechanism is based on the GEOS-Chem model, with anthropogenic emissions adopted from the Multiresolution Emission Inventory for China (MEIC) and biogenic isoprene emissions from the Model of Emissions of Gases and Aerosols from Nature (MEGAN) (Guenther et al., 2012). For our study, we run a REAM simulation for March and April 2018 to obtain a priori profiles of NO_2 and HCHO.

To ensure consistency in our intercomparisons of different products (Bucsela et al., 2008; Lamsal et al., 2014), we calculated AMFs using REAM a priori profiles (AMF_{REAM}) as $AMF_{REAM} = \frac{\sum_i V_{i,REAM} W_i}{\sum_i V_{i,REAM}}$, where $V_{i,REAM}$ is the VCD for vertical layer i, and W_i is the scattering weight for that layer. While NASA products provide the scattering weight data, the other products offer AVKs. The scattering weight vector (**W**) can be computed as $\mathbf{W} = \mathbf{AVK} * AMF$, where the AVKs are multiplied by the tropospheric AMF (Eskes & Boersma, 2003).

Studies have suggested a low bias in TROPOMI NO_2 product up to v1.3 due to cloud pressure retrieval biases (Griffin et al., 2019; Riess et al., 2022). However, the newer versions (since v1.4) with the updated cloud algorithms (van Geffen et al., 2022; P. Wang et al., 2008) do not cover our study period (March–April 2018). Therefore, for the TROPOMI NO_2 product, we performed cloud pressure corrections by replacing the original cloud pressure data with those provided by either of the two OMI products. The AMF of a partially clouded pixel is calculated as a linear combination of a cloudy AMF (AMF_{cld}), computed with corrected cloud pressures, and a clear AMF (AMF_{clr}), as shown in Equation 2, where f_r is the cloud radiance fraction (CRF) (Belmonte Rivas et al., 2015; Boersma et al., 2004). On TROPOMI cloudy days, that is, when TROPOMI cloud radiance fraction >0, the mean cloud pressures for OMI-NASA, OMI-KNMI, and TROPOMI v1.0.1 are 800, 674, and 953 hPa, respectively (Figure S2 in Supporting Information S1). On days when the specific OMI cloud data is not available, we used a scaling factor, which is the ratio between cloud pressures of OMI to TROPOMI, 0.8 for OMI-NASA and 0.7 for OMI-KNMI, to scale the TROPOMI cloud pressures. The relative change of NO_2 TVCDs, due to different selections of OMI cloud pressures, was 2.5%, a considerably smaller change compared to the 29.7% shift observed before and after applying cloud correction (Figure S3 in Supporting Information S1). Despite the OMI-KNMI's lower mean cloud pressure compared to OMI-NASA, the impact of OMI cloud pressure choices on the results appears relatively insignificant in comparison to the substantial change due to cloud correction. For the following analysis, we will use TROPOMI products that have been corrected by corresponding OMI-NASA cloud pressure data.

$$AMF = f_r AMF_{cld} + (1 - f_r) AMF_{clr} \quad (2)$$

During the measurement period, local agricultural burning occurred (Lee et al., 2021). To identify these burning events around the observation site, we utilized data from the Fire Information for Resource Management System (FIRMS) standard product (Davies et al., 2009). The FIRMS fire/hotspot data are derived from satellite sensors, including the Moderate Resolution Imaging Spectroradiometer (MODIS) onboard the Aqua and Terra satellites and the Visible Infrared Imaging Radiometer Suite (VIIRS) aboard S-NPP. By examining fire hot spots within 5 km of the observation site (Figure S4 in Supporting Information S1), we identified days affected by the burning events nearby. Since the emissions from these nearby fire events can potentially affect MAX-DOAS observations, we excluded the observations on 7 burning days from the intercomparisons between MAX-DOAS and satellite products. In Section 3.3, we further examine the effects of burning on trace gas and aerosol concentrations specifically on the two largest burning days, March 25 and April 11, using MAX-DOAS observations.

3. Results and Discussion

3.1. Overview of the Observations and Intercomparisons

Figure 2 illustrates the daily variations and uncertainties of NO_2 and HCHO TVCDs from MAX-DOAS and satellite products during the study period. Satellite data in the pixel over the site are compared to MAX-DOAS data at 13:00–14:00. The measured NO_2 TVCDs from MAX-DOAS ranged from 2×10^{15} to 1.8×10^{16} molecules/cm^2. In comparison to MAX-DOAS data, satellite observations captured the daily variations of NO_2 TVCDs well, except for a high bias in the OMI-NASA product. In contrast, larger discrepancies between MAX-DOAS and

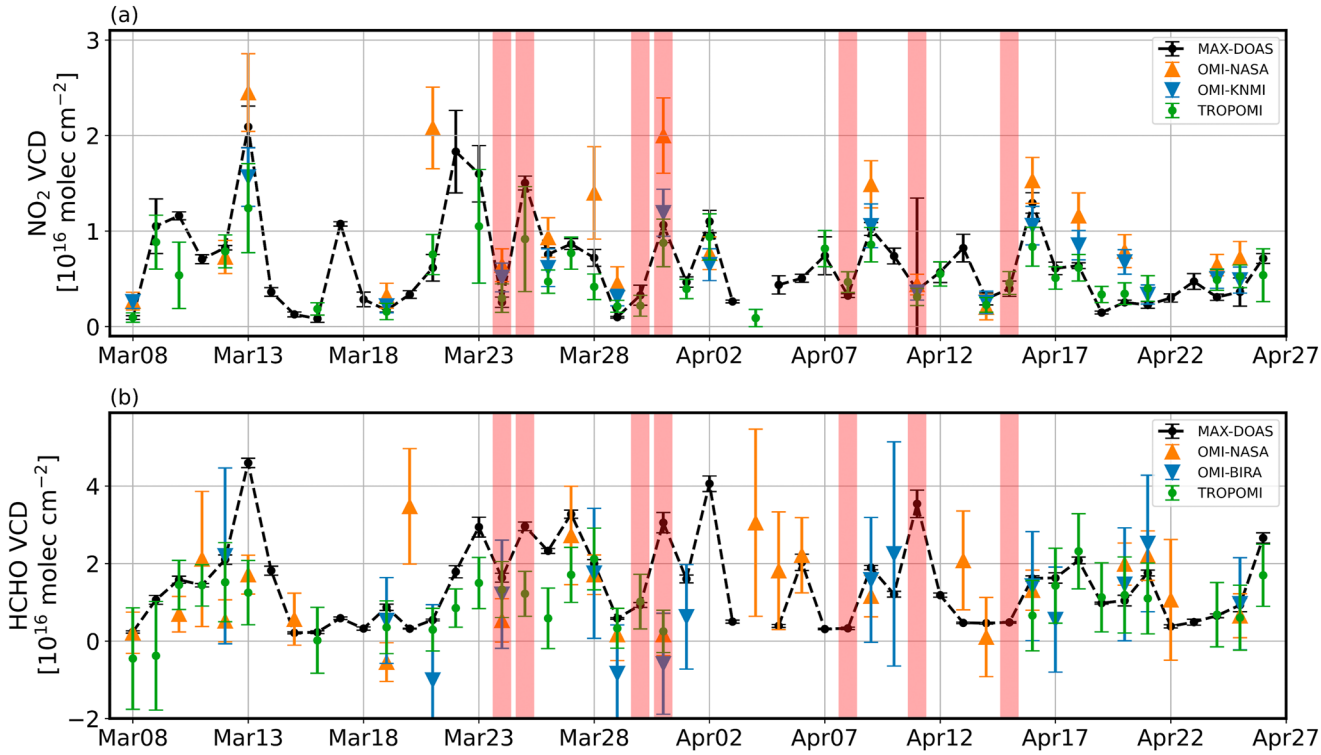

Figure 2. Daily variations and uncertainties (vertical error bars) of TVCDs from March 8 to April 26. (a) Time series of daily NO_2 TVCD data from MAX-DOAS (black), OMI-NASA (orange), OMI-KNMI (blue), and TROPOMI (green). (b) Time series of daily HCHO TVCD data from MAX-DOAS (black), OMI-NASA (orange), OMI-BIRA (blue), and TROPOMI (green). The red shadings indicate days affected by nearby burning activities.

satellite data were found for HCHO, accompanied by larger uncertainties as well. Comparison statistics including correlation coefficients (r), p-values for linear correlation tests, slope for the through-the-origin least squares regression, root mean square error (RMSE), mean bias error (MBE), and number of data pairs compared (N) are listed for each pair of comparison in Tables S2 and S3 in Supporting Information S1.

The intercomparisons between MAX-DOAS and three satellite NO_2 TVCD products are presented in Figure 3. Each data point represents a pair of satellite-MAX-DOAS measurements, and through-the-origin least-squares regression lines are shown for all comparisons. While the satellite data captured the daily variations well, noticeable biases can be seen. Specifically, OMI-KNMI and TROPOMI exhibited low biases compared to MAX-DOAS, whereas OMI-NASA showed a high bias (Figure 3a). These biases could be contributed by the differences in the a priori profiles used in the respective satellite products. We applied AMF_{REAM} computed from the same REAM a priori profiles to scale the original data products. For the two OMI products, the inclusion of AMF_{REAM} increased NO_2 TVCDs (Figure S3 in Supporting Information S1) due to a larger gradient of NO_2 concentrations from the lower boundary layer to the free troposphere simulated by the REAM model than the global model results used in the original satellite products, which was also reported in previous studies (Johnson et al., 2023). However, in the case of TROPOMI retrievals, the largest corrections are related to cloud pressure corrections to this specific version of TROPOMI data used in our study, as mentioned in the previous section, which resulted in a 21% increase in TROPOMI NO_2 TVCDs (Figure S3 in Supporting Information S1) and brought TROPOMI data into close agreement with MAX-DOAS measurements. After these corrections, OMI-KNMI and TROPOMI TVCDs exhibited reasonably good agreement with MAX-DOAS, while OMI-NASA data showed a 30% higher bias (Figure 3b). We note that using the same a priori profiles did not completely eliminate the discrepancies between OMI-NASA and OMI-KNMI TVCDs. A further investigation into the differences between these two OMI NO_2 TVCD products will be discussed in Section 3.2. Despite the biases, the correlation coefficients between satellite products and MAX-DOAS measurements for NO_2 TVCDs are all above 0.8 with significant p-values (<0.05), confirming the statistically significant agreements between satellite data and MAX-DOAS (Figure S5 in Supporting Information S1).

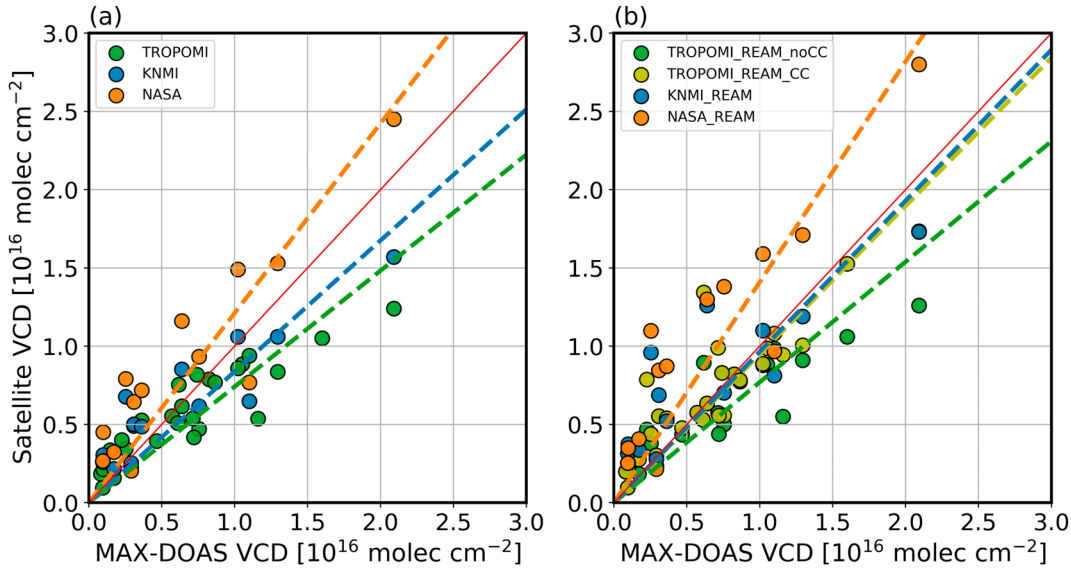

Figure 3. Intercomparison between NO_2 TVCDs from MAX-DOAS and those from satellites. (a) Before AMF adjustments, that is, OMI-NASA (orange), OMI-KNMI (blue), and TROPOMI (green). (b) After AMF corrections using AMF_{REAM}, that is, NASA_REAM (orange), KNMI_REAM (blue), and TROPOMI data with/without cloud correction (TROPOMI_REAM_CC/TROPOMI_REAM_noCC, olive/green). The dashed lines are least-squares regressions through the origin between satellite and MAX-DOAS data. A solid red line represents the 1:1 reference.

The discrepancies between MAX-DOAS and satellite HCHO products are much larger compared to the reasonable agreement observed among NO_2 products (Figure 4a). MAX-DOAS HCHO ranged from 2.3×10^{15} to 4.6×10^{16} molecules/cm^3. Correlations between standard satellite products and MAX-DOAS data are statistically insignificant ($p > 0.05$) (Figure S6 in Supporting Information S1), except for TROPOMI data, which exhibited a higher correlation coefficient (~0.6) and a significant correlation with MAX-DOAS data (p-value = 0.005). To address the impact of different a priori profiles, we corrected the satellite data with AMF_{REAM} calculated from REAM simulated a priori profiles. The correction significantly improved the correlation of OMI-NASA data with MAX-DOAS ($p < 0.05$) (Figure S6 in Supporting Information S1). However, the AMF_{REAM} effect on OMI-BIRA

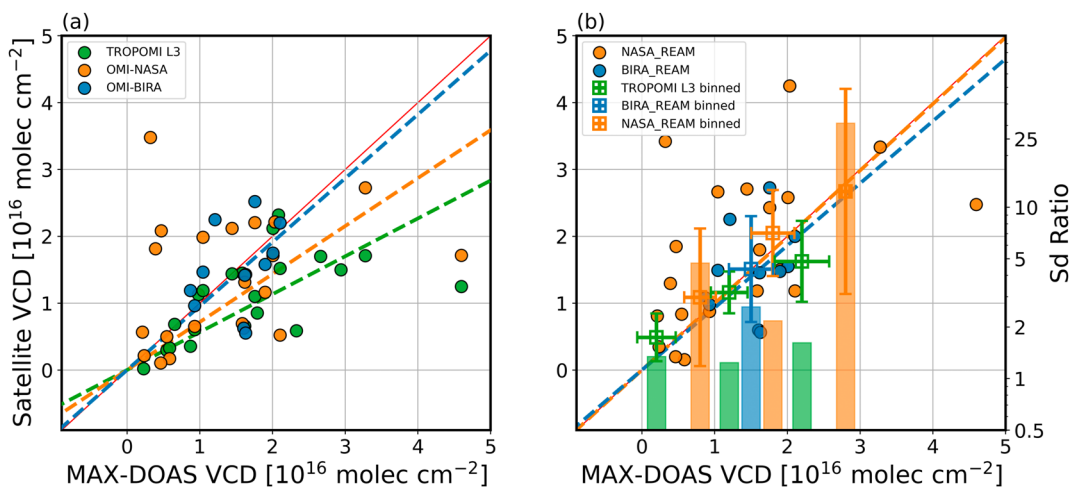

Figure 4. Intercomparison of HCHO TVCDs from MAX-DOAS with those from satellites. (a) OMI-NASA, OMI-BIRA, and TROPOMI data before AMF adjustment. (b) OMI-NASA and OMI-BIRA data after AMF adjustment. The boxes with error bars show the average and standard deviations for the corresponding variables in each bin of MAX-DOAS data. The vertical bars with standard deviations show the Sd ratio, the standard deviation ratios of satellite to MAX-DOAS data in each bin, in which more than 2 data points are available. The dashed lines are fitted on the corresponding scatter plots through the origin, with a solid red line representing the 1:1 reference.

data is negligible in the correlation comparison due to much better agreement of the OMI-BIRA AMF data with AMF_{REAM} than OMI-NASA AMF data (Figure S7 in Supporting Information S1). In the case of TROPOMI, since only L3 data is available, AMF adjustments could not be applied. To further quantify the comparisons, we analyzed the standard deviations of NASA_REAM, BIRA_REAM, and TROPOMI data. Binning the satellite data based on MAX-DOAS measurements, with each bin representing 10^{16} molecules/cm^2, we calculated the standard deviations of satellite and MAX-DOAS data when >2 data points are available. There are generally 6–9 data points in each bin, except for the comparison between OMI-NASA and MAX-DOAS, where the [2–3] $\times 10^{16}$ molecules/cm^2 bin only has three data points, resulting in a large standard deviation for that bin. Results showed that the standard deviations of OMI data are consistently larger than those of MAX-DOAS, whereas the standard deviations of TROPOMI are comparable to those of MAX-DOAS (Figure 4b), indicating better quality of TROPOMI HCHO data. Comparing the standard deviations of satellite data with those of MAX-DOAS data, for low-, mid-, and high-HCHO bins, the Sd ratios, are >3 for OMI data and ∼1 for TROPOMI data, indicating much improved correlation of TROPOMI data with MAX-DOAS data than that of OMI data. The examination of RMSE for the whole data set (Table S3 in Supporting Information S1) with roughly same sample sizes reveals that the RMSE for the OMI-NASA product is approximately twice that of the TROPOMI product.

Previous studies have also shown that intercomparisons of HCHO products generally exhibit larger scatters and weaker correlations compared to NO_2 products, especially in the case of OMI HCHO products (e.g., Johnson et al., 2023). This can be attributed to stronger Rayleigh scattering at shorter wavelengths (∼340 nm for HCHO) than at longer wavelengths (∼440 nm for NO_2), resulting in lower sensitivity of measurements to HCHO in the lower atmosphere than to NO_2 (Boersma et al., 2016). Although only pre-release TROPOMI HCHO data were available during the OPECE period, the analysis showed promising improvements in the signal-to-noise ratios of TROPOMI HCHO product compared to OMI (De Smedt et al., 2021). Furthermore, it should be noted that some scatter in the comparisons of satellite data with MAX-DOAS data can be caused by uncertainties related to spatial representativeness or mismatch and random uncertainties of satellite products, which are challenging to quantify from pairwise comparisons (Hubert et al., 2021). Estimating the random uncertainties may require a triple co-location method (Stoffelen, 1998), but this approach requires a larger data set than available in this study (e.g., sample size $N > 100$) (Dong & Crow, 2017; McColl et al., 2014; Zwieback et al., 2012). Nonetheless, the comparison of satellite HCHO TVCDs to NO_2 data based on MAX-DOAS observations is informative in demonstrating the larger uncertainties associated with satellite HCHO retrievals compared to NO_2.

During this study period, we investigated the weekly variations in MAX-DOAS and satellite TVCDs of NO_2 and HCHO to gain insights into potential source contributions of pollutants. Previous studies have suggested lower NO_2 TVCDs on weekends than on weekdays in urban regions (Beirle et al., 2003; Gu et al., 2014; J. Li et al., 2021; Shaiganfar et al., 2015; Stavrakou et al., 2020). However, the average weekly variation of NO_2 and HCHO data sets (Figure S8 in Supporting Information S1) did not exhibit statistically significant variations based on the Kruskal-Wallis test (Table S4 in Supporting Information S1). The lack of significant weekly variations can be attributed to the influence of changes in transport to the observation site, which can weaken the expected weekly cycle associated with urban emissions (Choi et al., 2012; Stavrakou et al., 2020; Y. Wang et al., 2019; Wang, Lampel, et al., 2017). Furthermore, MAX-DOAS observations of SO_2 (Figure S15 in Supporting Information S1) indicated that the rural observation site was strongly affected by the transport of polluted and clean air masses.

3.2. Resolving the Difference Between NASA and KNMI NO_2 TVCDs

We further investigated the systematically higher biases observed in OMI-NASA NO_2 TVCDs than in OMI-KNMI data. Examination of SCDs showed negligible discrepancies between these two products (Figure S9 in Supporting Information S1), consistent with previous studies (Compernolle et al., 2020; Zara et al., 2018). Therefore, our focus shifted to the difference in AMFs, which is known to be a major source of uncertainty in the OMI NO_2 retrievals (Lorente et al., 2017). A comparison of AMFs for the two OMI products before and after applying the REAM a priori profiles showed that using the same a priori profiles results in slightly better AMF agreement between NASA and KNMI data, but the substantial low bias in the NASA AMFs persisted (Figure 5). This result suggested that the difference in AMFs between the two OMI products is not primarily influenced by the difference in NO_2 a priori profiles but rather by the scattering weights, which are independent of the vertical distribution for optically thin absorbers like NO_2 (Laughner et al., 2016; Palmer et al., 2001).

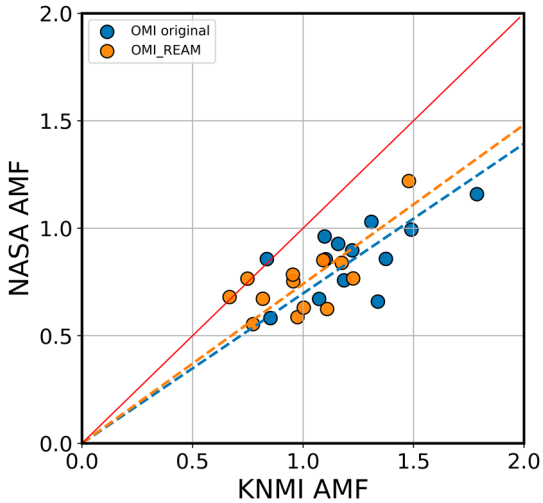

Figure 5. Scatter plots of original AMF (blue) and REAM profile scaled AMF_{REAM} (orange) from OMI-NASA versus OMI-KNMI. The dashed lines are least-squares regressions through the origin, and a solid red line represents the 1:1 reference.

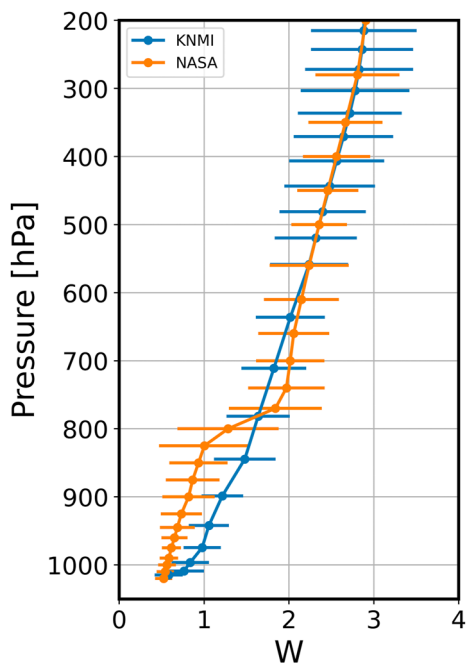

Figure 6. The median vertical profiles with standard deviations (horizontal error bars) of scattering weights (w) of OMI-NASA (orange) and OMI-KNMI (blue) products from March 8 to April 26.

Further inspection of scattering weights revealed a low bias of scattering weights of OMI-NASA compared to those of OMI-KNMI in the lower troposphere, specifically around 800 hPa (Figure 6). The scattering weights are determined through a look-up table based on factors including optical geometry, surface reflectivity, cloud pressure, and cloud fraction (Eskes & Boersma, 2003; Krotkov et al., 2017).

Cloud properties were compared between KNMI and NASA retrievals during the study period (Figure 7), revealing retrieved average cloud pressures of 645 ± 260 hPa for KNMI and 820 ± 115 hPa for NASA. In addition, the mean cloud radiance fraction from NASA is approximately 0.3, which is around twice as large as that of KNMI at around 0.15. This discrepancy in cloud properties between the two OMI products extends beyond the observation site, as shown by a comparison of mean distributions for the NCP region around the OPECE site (Figure S10 in Supporting Information S1). Surface reflectivity also affects AMF calculation by being one parameter used in the look-up table for scattering weights and indirectly through its impact on cloud retrievals (Boersma et al., 2018; Lorente et al., 2018). The v4.0 of the NASA product incorporated the geometry-dependent surface Lambertian equivalent reflectivity (GLER) product to account for the bidirectional reflectance distribution function (BRDF) effect. The daily GLER product is derived from MODIS observations and applied to both NO_2 and cloud retrievals in the NASA product, replacing the climatological OMI-based data sets used in previous versions (Fasnacht et al., 2019; Lamsal et al., 2021; Qin et al., 2019; Vasilkov et al., 2018). Studies have indicated that the inclusion of this new GLER product could lead to lower AMF by 29%–50% due to a combination of the BRDF effect and biases between MODIS and OMI-based data sets (Lamsal et al., 2021; Vasilkov et al., 2017). It remains unclear whether updating GLER in NASA retrievals is responsible for the observed differences in the scattering weight profiles in this study. Further inspections comparing the retrieval algorithms of two OMI products are needed. Additionally, since the observation site is coastal (Figure 1), lower-level clouds in the ocean boundary layer may also contribute to the uncertainties in AMF calculations (Boersma et al., 2004). Furthermore, both OMI-KNMI and OMI-NASA products accounted for scattering effects of aerosols in AMF calculations (Boersma et al., 2011; Lamsal et al., 2021). The aerosol optical depth (AOD) measured by MAX-DOAS during our study period is 1 ± 0.48. Absorbing aerosols might introduce further uncertainties (Leitão et al., 2010).

3.3. Biomass Burning Impacts on HONO, NO_2, and HCHO

During the measurement period, we identified 7 BB days using FIRMS fire hot spot data (Figure S4 in Supporting Information S1). Among these 7 days, the OMI products had around two valid measurements and TROPOMI had three valid measurements. Since agricultural burning is often localized, its impact can be much larger on the ground-based MAX-DOAS measurements than on OMI data. TROPOMI data has a finer horizontal resolution than OMI data (Theys et al., 2020), but is not publicly available during our study period, when TROPOMI was still in the commissioning phase. Additionally, the MAX-DOAS instrument provides vertical profile information. Therefore, only the MAX-DOAS measurements are utilized in the analysis of BB impacts.

On the BB days, westerly winds at ~3 m/s dominated the site, except for March 25, April 8, and April 11. The MAX-DOAS observations of SO_2, HONO, HCHO, NO_2, and AEC for all the BB days (Figure S11 in Supporting Information S1) indicated significant variations in air quality conditions. The daytime mixing ratios of SO_2 ranged from 0.4 to 9.2 ppbV. The

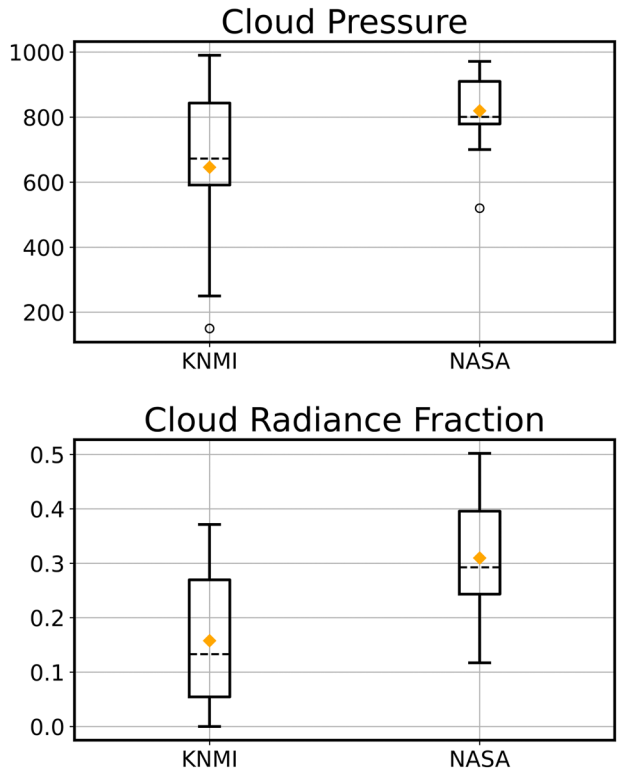

Figure 7. Box plots for cloud pressure (hPa, upper row) and cloud radiance fraction (unitless, lower row) of OMI-KNMI and OMI-NASA on all quality flag filtered days in this study.

enhancements of NO_2 and HCHO tend to occur concurrently. These enhancements also correlate with the occurrences of HONO enhancements, but to a lesser degree. On the other hand, AEC concentrations can be enhanced even when NO_2 and HCHO concentrations are not elevated, reflecting likely aerosol production during the smoldering stage of burning and subsequent transport processes.

The observations of SO_2 indicated that BB events occurred on both polluted and clean days. In order to accurately quantify BB enhancements, it is important to account for the background concentrations. To achieve this, we utilized the observed SO_2 concentrations to distinguish between clean and polluted days. Specifically, days with noontime near-surface SO_2 lower than 1 ppbV were identified as clean days while others were classified as polluted. During the measurement period, we identified 12 clean days and 38 polluted days based on this criterion.

For BB effect analysis, we divided the observations into two groups based on the pollution conditions and selected two BB days with the highest fire counts under clean (April 11) and polluted (March 25) conditions, respectively. Other than the highest fire counts, these two days were also characterized by elevated HCHO and NO_2 in the upper boundary layer compared to other BB days, indicating more pronounced BB impacts (Figure S11 in Supporting Information S1). On March 25, significant burning activities occurred 5 km to the west of the site. Wind at 3 m/s came from the northwest. On April 11, wind was weak at 0.7 m/s, and the burnings occurred right next to the site (Figure S12 in Supporting Information S1).

Figure 8 illustrates the daytime profiles of trace gas species and AEC for both BB events and their corresponding average background conditions. On average, polluted days exhibited much higher boundary-layer concentrations than clean days for all species, except for HONO.

On April 11, observed SO_2 concentrations surpassed the average levels of non-BB days, indicating that BB could also contribute to the observed high concentrations. Notably, observations of HCHO revealed three distinct burning plumes reaching above 0.5 km between 1 and 6 p.m. LT, accompanied by corresponding enhancements in NO_2, peaking above 0.5 km around 2 p.m. LT. The observations of HONO displayed significant enhancements up to 1.2 km from 1 to 3 p.m. LT, marking the largest HONO pollution event throughout the campaign (Figure S13 in Supporting Information S1). Additionally, observations of AEC on April 11 also showed elevated levels up to 1.5 km between 1 and 3 p.m. LT, with high AEC concentrations limited to the lower boundary layer in the late afternoon. These observations are consistent with photolytically enhanced production of HONO on aerosols, as discussed in previous studies (Z. Liu et al., 2014; Ye et al., 2016).

On March 25, higher SO_2 concentrations were also observed in the lower boundary layer compared to the average non-BB polluted days. HCHO observations showed elevated concentrations at 0.5–1 km throughout the day, while NO_2 observations exhibited elevated levels, with larger enhancements in the late morning than in the afternoon. It is noteworthy that the average vertical gradient of NO_2 is larger than that of HCHO on polluted non-BB days (Figure S14 in Supporting Information S1), reflecting the secondary production of HCHO (Alvarado et al., 2020). However, the enhancements of HONO and AEC on March 25 were not as significant as those of HCHO and NO_2 compared to the average non-BB days.

During the flaming stage, HONO can be co-emitted with NO_x (Roberts et al., 2020), whereas during the smoldering stage, the secondary production of HONO becomes more important (Peng et al., 2022). Heterogeneous HONO production mechanisms have been extensively studied in recent years due to their potentially significant impact on O_3 production, such as photo-enhanced NO_2 conversion on aerosols (Z. Liu et al., 2014) and the photolysis of particulate nitrate (Ye et al., 2016). Among HONO, NO_2, and HCHO, HONO has the shortest photochemical lifetime. Therefore, the moderate but more persistent enhancements of HONO than those of NO_2 and

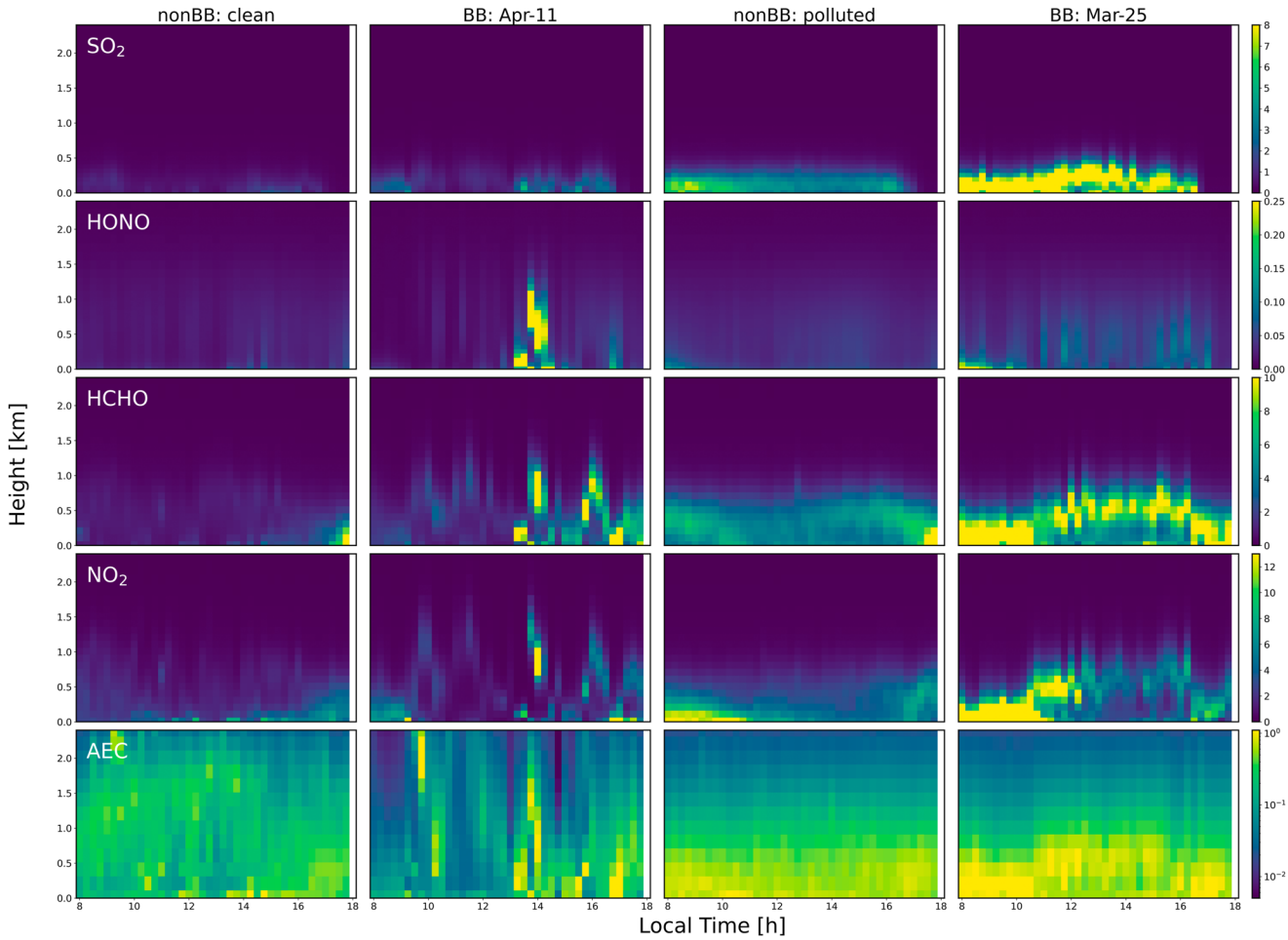

Figure 8. MAX-DOAS observed daytime evolutions of SO_2, HONO, HCHO, NO_2, and AEC mixing ratios for (a) non-burning days under clean conditions, (b) on April 11, during the burning events under clean conditions, (c) non-burning days under polluted conditions, and (d) on March 25, during the burning events under polluted conditions.

HCHO throughout the boundary layer on March 25 (Figure 8) likely reflects heterogeneous HONO production that sustained the elevated level of HONO.

To quantify the enhancements due to BB at both the surface and upper layers, we determined the height of the surface mixed layer by the location of the largest SO_2 vertical gradient on polluted days. For clean days, the average hourly height of the surface mixed layer height was used. The derived surface layer heights during the OPECE experiment ranged from 300 to 500 m (Figure S15 in Supporting Information S1). To assess the BB enhancements, we integrated MAX-DOAS observations within the lower columns of the surface mixed layer and the upper columns from the top of the surface layer to 3.5 km. Subsequently, we calculated the column enhancement ratios, denoted as X, of lower and upper columns on the selected burning days to the corresponding averages on non-BB days, that is, April 11 data relative to non-BB clean days' average and March 25 to the non-BB polluted days' average. Figures 9a and 9b shows the ratios of NO_2, HONO, HCHO, AEC, and SO_2 column enhancements. The column enhancement ratios for SO_2, Xso_2, are large in both the upper and lower columns on April 11 and in the lower column on March 25. The polluted NCP region is characterized by high anthropogenic SO_2 emissions (Fu et al., 2016; Xu et al., 2011). Additionally, agricultural burning also contributes to SO_2 emissions. The emission factor ratio of SO_2 to NO_2 for agricultural fires is estimated to be 0.4 (X. Liu et al., 2016). However, as shown in Figure 8, the observed SO_2 concentrations do not correlate with NO_2, which is produced during BB, on burning days. Figure 9 further demonstrates that the X_{SO2} is much larger than X_{NO2} in the surface mixed layer on two BB days, indicating that relative enhancement ratios of SO_2 to NO_2 are much larger than the emission factor for agricultural burning reported by X. Liu et al. (2016). Consequently, the observational evidence suggests that BB emissions of SO_2 are negligible compared to other anthropogenic SO_2 sources at the observation site.

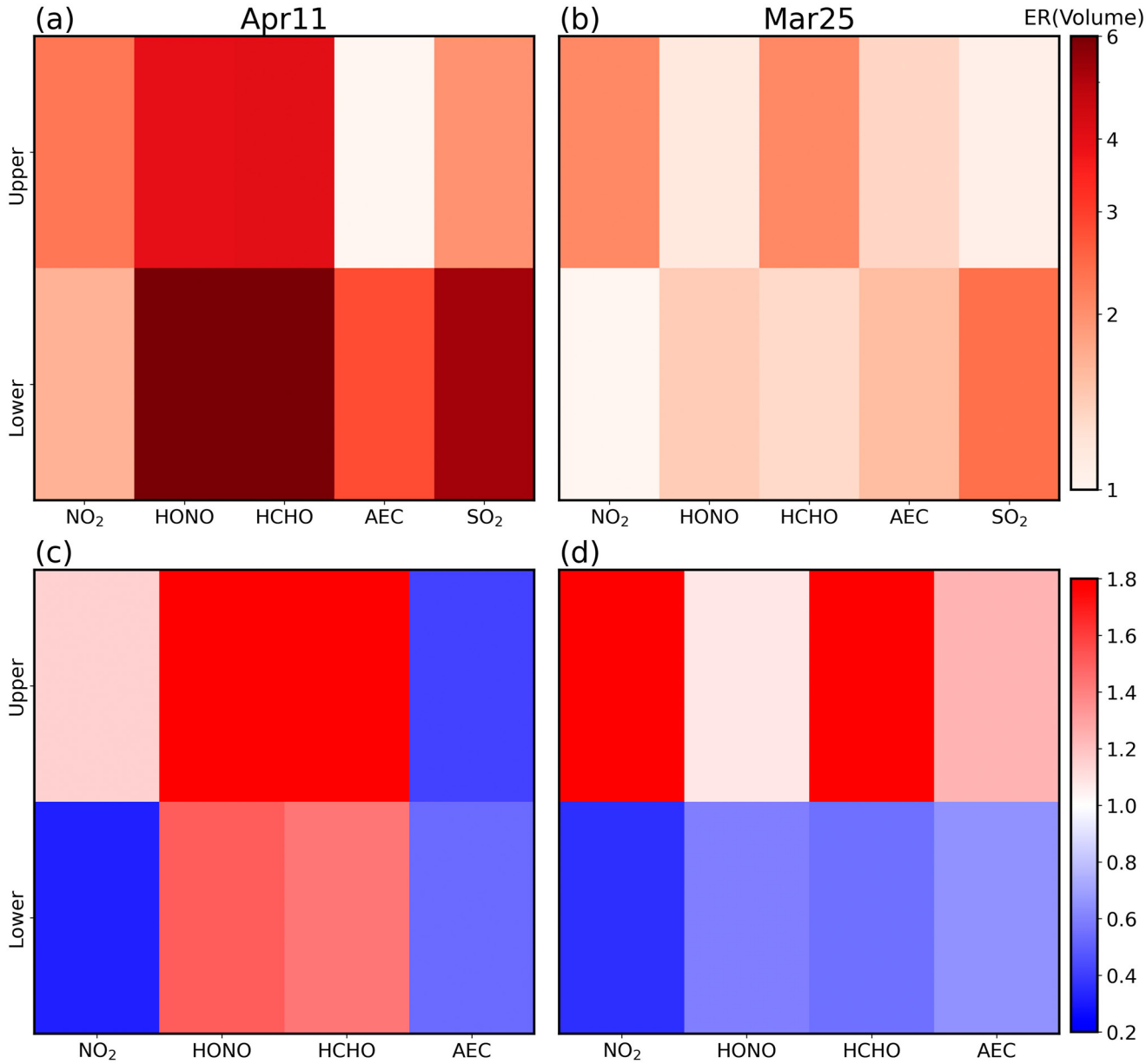

Figure 9. (a) Enhancement ratios of BB to non-BB days of NO_2, HONO, HCHO, AEC, and SO_2 in the upper and lower columns for April 11. (b) Same as (a) but for March 25. (c) BB enhancement ratios relative to SO_2 enhancement in the upper and lower columns for NO_2, HONO, HCHO, and AEC for April 11. (d) Same as (c) but for March 25. See text for details.

Since SO_2 is not affected by BB emissions, we calculated BB enhancements relative to that of SO_2 given the nearly linear relationships of the non-BB enhancements of other species with that of SO_2 (Figure S16 in Supporting Information S1). This can be expressed as the relative BB enhancement ratio: $\frac{X^i/X^i_{bg}}{X^{SO_2}/X^{SO_2}_{bg}}$, where X^i denotes the density of species i, and X^i_{bg} denotes the average density of species i on the corresponding non-BB days. Figures 9c and 9d show the relative BB enhancement ratios for April 11 and March 25. In the surface layer, the relative BB enhancement ratios of all species are either slightly greater than 1 or less than 1. However, in the upper layer, the enhancements of HONO, NO_2, and HCHO are larger compared to the surface layer, indicating stronger vertical transport due to the higher potential temperature of fresh BB air masses during the flaming stage, caused by fire heating. Another supporting piece of evidence for fires in the flaming stage is that the

relative enhancement ratios of AEC in the upper layer are small, in contrast to the large enhancement of PMs accompanying the smoldering combustion (Chakrabarty et al., 2010; Urbanski, 2013). On these 2 days with the highest fire counts during the OPECE experiment, the fire enhancement of HCHO in the upper layer is consistently large, while HONO and NO_2 enhancement ratios are comparably large only on one of the days. The four panels of Figure 9 together reveal that HCHO and NO_2 enhancements in the upper layer tend to occur together but the enhancement magnitudes have large variations. In comparison, the patterns of HONO enhancements differ from those of HCHO and NO_2.

4. Conclusions

Satellite NO_2 and HCHO products provide valuable insights into pollution distributions and global photochemistry. However, to ensure their accurate applications, the validation of satellite products is essential. Ground-based observations conducted at rural sites with minimal local emissions are particularly useful for this purpose. In this study, we utilized MAX-DOAS observations collected at a rural coastal site in Dongying, China, during the OPECE experiment. The MAX-DOAS observations of NO_2 and HCHO on days without local burnings are intercompared with NASA and KNMI OMI and TROPOMI operational NO_2 TVCD products, NASA and BIRA OMI HCHO products, and TROPOMI L3 HCHO products. Additionally, we analyzed the effects of BB on boundary layer HONO, NO_2, and HCHO using MAX-DOAS observations on days with local burnings.

After employing consistent a priori profiles from the regional REAM model in OMI and MAX-DOAS retrievals and correcting the cloud pressure bias in TROPOMI v1.0 retrievals, we found a generally better agreement of satellite with MAX-DOAS data for NO_2 products than for HCHO products. When comparing with MAX-DOAS data, the correlation coefficients for all satellite NO_2 products exceeded 0.8. While OMI-KNMI and TROPOMI data exhibit no significant biases, OMI-NASA data showed a ∼30% positive bias. Further analysis indicated that this bias is due to a lower estimation of scattering weight profiles in the lower troposphere in the OMI-NASA NO_2 product than in the OMI-KNMI data. The reasons for this discrepancy could be attributed in part to the more extensive cloud presence above the boundary layer around the observation site in the OMI-NASA than OMI-KNMI products. On the other hand, the agreement between satellite and MAX-DOAS HCHO data was relatively low, with correlation coefficients below 0.6. The TROPOMI HCHO data exhibited the highest correlation coefficient and significantly lower data scattering relative to MAX-DOAS data compared to OMI data. This intercomparison suggests that the TROPOMI HCHO product shows good promise for improvement compared to OMI.

MAX-DOAS observed vertical profiles of SO_2 show that the observation site was affected by the transport of polluted and clean air masses. We used these data to categorize the observations into clean and polluted days and to estimate the heights of the surface mixed layer. Analysis of MAX-DOAS observations on the two largest burning days (March 25 and April 11) revealed more pronounced enhancements due to fire emissions in the upper boundary layer than the surface mixed layer, reflecting the higher potential temperature of fresh burning air masses due to fire heating during the flaming stage. The evident upper boundary fire enhancements and comparatively lower enhancements of AEC than NO_2 and HCHO are consistent with the prevalent influence of flaming combustions in MAX-DOAS measurements, which are limited to daytime only. Concentrations of HONO, NO_2, and HCHO can be substantially enhanced by burning, with NO_2 and HCHO enhancements often occurring together but exhibiting considerable variations in magnitude. On the other hand, the fire enhancements of HONO exhibit noticeable differences compared to those of HCHO and NO_2, and they also demonstrate a higher level of variability.

Data Availability Statement

The vertical profiles of NO_2, SO_2, HONO, HCHO, and AEC from MAX-DOAS measurements can be found at (Chong et al., 2023). The satellite data sets used in this study are available in the following links or references: (a) OMI-NASA NO_2 (Krotkov et al., 2019a, 2019b); (b) OMI-KNMI NO_2 (Boersma et al., 2011; KNMI, 2011); (c) TROPOMI NO_2 (CopernicusSentinel-5P, 2018); (d) OMI-NASA HCHO at (Chance, 2007); (e) OMI-BIRA HCHO (De Smedt et al., 2017). The TROPOMI L3 HCHO data is obtained from a previous study (De Smedt et al., 2021).

Acknowledgments
The authors acknowledge Dr. Isabelle De Smedt for providing daily L3 TROPOMI HCHO data from BIRA-IASB. This work is supported by the National Science Foundation Atmospheric Chemistry Program (Grant 1743401). The authors thank the science team of the OPECE 2018 campaign.

References

Alvarado, L. M. A., Richter, A., Vrekoussis, M., Hilboll, A., Kalisz Hedegaard, A. B., Schneising, O., & Burrows, J. P. (2020). Unexpected long-range transport of glyoxal and formaldehyde observed from the Copernicus Sentinel-5 Precursor satellite during the 2018 Canadian wildfires. *Atmospheric Chemistry and Physics*, *20*(4), 2057–2072. https://doi.org/10.5194/acp-20-2057-2020

Balamurugan, V., Chen, J., Qu, Z., Bi, X., Gensheimer, J., Shekhar, A., et al. (2021). Tropospheric NO_2 and O_3 response to COVID-19 lockdown restrictions at the National and Urban scales in Germany. *Journal of Geophysical Research: Atmospheres*, *126*(19), e2021JD035440. https://doi.org/10.1029/2021JD035440

Beirle, S., Platt, U., Wenig, M., & Wagner, T. (2003). Weekly cycle of NO_2 by GOME measurements: A signature of anthropogenic sources. *Atmospheric Chemistry and Physics*, *3*(6), 2225–2232. https://doi.org/10.5194/acp-3-2225-2003

Belmonte Rivas, M., Veefkind, P., Eskes, H., & Levelt, P. (2015). OMI tropospheric NO_2 profiles from cloud slicing: Constraints on surface emissions, convective transport and lightning NO_x. *Atmospheric Chemistry and Physics*, *15*(23), 13519–13553. https://doi.org/10.5194/acp-15-13519-2015

Boersma, K. F., Eskes, H. J., & Brinksma, E. J. (2004). Error analysis for tropospheric NO_2 retrieval from space. *Journal of Geophysical Research*, *109*(D4), D04311. https://doi.org/10.1029/2003JD003962

Boersma, K. F., Eskes, H. J., Dirksen, R. J., van der A, R. J., Veefkind, J. P., Stammes, P., et al. (2011). An improved tropospheric NO_2 column retrieval algorithm for the ozone monitoring instrument. *Atmospheric Measurement Techniques*, *4*(9), 1905–1928. https://doi.org/10.5194/amt-4-1905-2011

Boersma, K. F., Eskes, H. J., Richter, A., De Smedt, I., Lorente, A., Beirle, S., et al. (2018). Improving algorithms and uncertainty estimates for satellite NO_2 retrievals: Results from the quality assurance for the essential climate variables (QA4ECV) project. *Atmospheric Measurement Techniques*, *11*(12), 6651–6678. https://doi.org/10.5194/amt-11-6651-2018

Boersma, K. F., Geffen, J. V., Eskes, H., A, R. V. D., Smedt, I. D., Roozendael, M. V., et al. (2017). In *Product specification document for the QA4ECV NO2 ECV precursor product 1.1*.

Boersma, K. F., Vinken, G. C. M., & Eskes, H. J. (2016). Representativeness errors in comparing chemistry transport and chemistry climate models with satellite UV–Vis tropospheric column retrievals. *Geoscientific Model Development*, *9*(2), 875–898. https://doi.org/10.5194/gmd-9-875-2016

Bucsela, E. J., Krotkov, N. A., Celarier, E. A., Lamsal, L. N., Swartz, W. H., Bhartia, P. K., et al. (2013). A new stratospheric and tropospheric NO_2 retrieval algorithm for nadir-viewing satellite instruments: Applications to OMI. *Atmospheric Measurement Techniques*, *6*(10), 2607–2626. https://doi.org/10.5194/amt-6-2607-2013

Bucsela, E. J., Perring, A. E., Cohen, R. C., Boersma, K. F., Celarier, E. A., Gleason, J. F., et al. (2008). Comparison of tropospheric NO_2 from in situ aircraft measurements with near-real-time and standard product data from OMI. *Journal of Geophysical Research*, *113*(D16), D16S31. https://doi.org/10.1029/2007JD008838

Chakrabarty, R. K., Moosmüller, H., Chen, L. W. A., Lewis, K., Arnott, W. P., Mazzoleni, C., et al. (2010). Brown carbon in tar balls from smoldering biomass combustion. *Atmospheric Chemistry and Physics*, *10*(13), 6363–6370. https://doi.org/10.5194/acp-10-6363-2010

Chance, K. (2007). In *OMI/Aura formaldehyde (HCHO) total column 1-orbit L2 Swath 13 × 24 km version V003*. https://doi.org/10.5067/Aura/OMI/DATA2015

Choi, Y., Kim, H., Tong, D., & Lee, P. (2012). Summertime weekly cycles of observed and modeled NO_x and O_3 concentrations as a function of satellite-derived ozone production sensitivity and land use types over the Continental United States. *Atmospheric Chemistry and Physics*, *12*(14), 6291–6307. https://doi.org/10.5194/acp-12-6291-2012

Chong, K., Wang, Y., Liu, C., Gao, Y., Boersma, K. F., Tang, J., & Wang, X. (2023). Vertical profiles retrieved from MAX-DOAS and REAM simulation output figshare. https://doi.org/10.6084/m9.figshare.23118890.v1

Compernolle, S., Verhoelst, T., Pinardi, G., Granville, J., Hubert, D., Keppens, A., et al. (2020). Validation of Aura-OMI QA4ECV NO_2 climate data records with ground-based DOAS networks: The role of measurement and comparison uncertainties. *Atmospheric Chemistry and Physics*, *20*(13), 8017–8045. https://doi.org/10.5194/acp-20-8017-2020

Copernicus Sentinel-5P. (2018). *TROPOMI level 2 nitrogen dioxide total column products version 01*. European Space Agency. https://doi.org/10.5270/S5P-s4ljg54

Danckaert, T., Fayt, C., Van Roozendael, M., De Smedt, I., Letocart, V., Merlaud, A., & Pinardi, G. (2012). QDOAS software user manual.

Davies, D. K., Ilavajhala, S., Wong, M. M., & Justice, C. O. (2009). Fire information for resource management system: Archiving and distributing MODIS active fire data. *IEEE Transactions on Geoscience and Remote Sensing*, *47*(1), 72–79. https://doi.org/10.1109/TGRS.2008.2002076

De Smedt, I., Pinardi, G., Vigouroux, C., Compernolle, S., Bais, A., Benavent, N., et al. (2021). Comparative assessment of TROPOMI and OMI formaldehyde observations and validation against MAX-DOAS network column measurements. *Atmospheric Chemistry and Physics*, *21*(16), 12561–12593. https://doi.org/10.5194/acp-21-12561-2021

De Smedt, I., Stavrakou, T., Hendrick, F., Danckaert, T., Vlemmix, T., Pinardi, G., et al. (2015). Diurnal, seasonal and long-term variations of global formaldehyde columns inferred from combined OMI and GOME-2 observations. *Atmospheric Chemistry and Physics*, *15*(21), 12519–12545. https://doi.org/10.5194/acp-15-12519-2015

De Smedt, I., Theys, N., Yu, H., Danckaert, T., Lerot, C., Compernolle, S., et al. (2018). Algorithm theoretical baseline for formaldehyde retrievals from S5P TROPOMI and from the QA4ECV project. *Atmospheric Measurement Techniques*, *11*(4), 2395–2426. https://doi.org/10.5194/amt-11-2395-2018

De Smedt, I., Yu, H., Richter, A., Beirle, S., Eskes, H., Boersma, K. F., et al. (2017). QA4ECV HCHO tropospheric column data from OMI version 1.1. [Value]. https://doi.org/10.18758/71021031

DiMaria, C. A., Jones, D. B. A., Worden, H., Bloom, A. A., Bowman, K., Stavrakou, T., et al. (2023). Optimizing the isoprene emission model MEGAN with satellite and ground-based observational constraints. *Journal of Geophysical Research: Atmospheres*, *128*(4), e2022JD037822. https://doi.org/10.1029/2022JD037822

Dong, J., & Crow, W. T. (2017). An improved triple collocation analysis algorithm for decomposing autocorrelated and white soil moisture retrieval errors. *Journal of Geophysical Research: Atmospheres*, *122*(24), 13081–13094. https://doi.org/10.1002/2017JD027387

Douglass, A. R., Stolarski, R. S., Strahan, S. E., & Connell, P. S. (2004). Radicals and reservoirs in the GMI chemistry and transport model: Comparison to measurements. *Journal of Geophysical Research*, *109*(D16), D16302. https://doi.org/10.1029/2004JD004632

Dovrou, E., Bates, K. H., Moch, J. M., Mickley, L. J., Jacob, D. J., & Keutsch, F. N. (2022). Catalytic role of formaldehyde in particulate matter formation. *Proceedings of the National Academy of Sciences of the United States of America*, *119*(6), e2113265119. https://doi.org/10.1073/pnas.2113265119

Eskes, H. J., & Boersma, K. F. (2003). Averaging kernels for DOAS total-column satellite retrievals. *Atmospheric Chemistry and Physics*, *3*(5), 1285–1291. https://doi.org/10.5194/acp-3-1285-2003

Fasnacht, Z., Vasilkov, A., Haffner, D., Qin, W., Joiner, J., Krotkov, N., et al. (2019). A geometry-dependent surface Lambertian-equivalent reflectivity product for UV–Vis retrievals—Part 2: Evaluation over open ocean. *Atmospheric Measurement Techniques*, *12*(12), 6749–6769. https://doi.org/10.5194/amt-12-6749-2019

Felix, J. D., & Elliott, E. M. (2014). Isotopic composition of passively collected nitrogen dioxide emissions: Vehicle, soil and livestock source signatures. *Atmospheric Environment*, *92*, 359–366. https://doi.org/10.1016/j.atmosenv.2014.04.005

Finlayson, B. J., & Pitts, J. N. (1976). Photochemistry of the polluted troposphere. *Science*, *192*(4235), 111–119. https://doi.org/10.1126/science.192.4235.111

Frieß, U., Klein Baltink, H., Beirle, S., Clémer, K., Hendrick, F., Henzing, B., et al. (2016). Intercomparison of aerosol extinction profiles retrieved from MAX-DOAS measurements. *Atmospheric Measurement Techniques*, *9*(7), 3205–3222. https://doi.org/10.5194/amt-9-3205-2016

Fu, X., Wang, S., Chang, X., Cai, S., Xing, J., & Hao, J. (2016). Modeling analysis of secondary inorganic aerosols over China: Pollution characteristics, and meteorological and dust impacts. *Scientific Reports*, *6*(1), 1–7. https://doi.org/10.1038/srep35992

González Abad, G., Liu, X., Chance, K., Wang, H., Kurosu, T. P., & Suleiman, R. (2015). Updated smithsonian astrophysical observatory ozone monitoring instrument (SAO OMI) formaldehyde retrieval. *Atmospheric Measurement Techniques*, *8*(1), 19–32. https://doi.org/10.5194/amt-8-19-2015

González Abad, G., Vasilkov, A., Seftor, C., Liu, X., & Chance, K. (2016). Smithsonian astrophysical observatory ozone mapping and profiler suite (SAO OMPS) formaldehyde retrieval. *Atmospheric Measurement Techniques*, *9*(7), 2797–2812. https://doi.org/10.5194/amt-9-2797-2016

Griffin, D., Zhao, X., McLinden, C. A., Boersma, F., Bourassa, A., Dammers, E., et al. (2019). High-resolution mapping of nitrogen dioxide with TROPOMI: First results and validation over the Canadian oil sands. *Geophysical Research Letters*, *46*(2), 1049–1060. https://doi.org/10.1029/2018GL081095

Gu, D., Wang, Y., Smeltzer, C., & Boersma, K. F. (2014). Anthropogenic emissions of NO_x over China: Reconciling the difference of inverse modeling results using GOME-2 and OMI measurements. *Journal of Geophysical Research: Atmospheres*, *119*(12), 7732–7740. https://doi.org/10.1002/2014JD021644

Guenther, A. B., Jiang, X., Heald, C. L., Sakulyanontvittaya, T., Duhl, T., Emmons, L. K., & Wang, X. (2012). The model of emissions of gases and aerosols from nature version 2.1 (MEGAN2.1): An extended and updated framework for modeling biogenic emissions. *Geoscientific Model Development*, *5*(6), 1471–1492. https://doi.org/10.5194/gmd-5-1471-2012

Hendrick, F., Müller, J. F., Clémer, K., Wang, P., De Mazière, M., Fayt, C., et al. (2014). Four years of ground-based MAX-DOAS observations of HONO and NO_2 in the Beijing area. *Atmospheric Chemistry and Physics*, *14*(2), 765–781. https://doi.org/10.5194/acp-14-765-2014

Hönninger, G., von Friedeburg, C., & Platt, U. (2004). Multi axis differential optical absorption spectroscopy (MAX-DOAS). *Atmospheric Chemistry and Physics*, *4*(1), 231–254. https://doi.org/10.5194/acp-4-231-2004

Hubert, D., Heue, K. P., Lambert, J. C., Verhoelst, T., Allaart, M., Compernolle, S., et al. (2021). TROPOMI tropospheric ozone column data: Geophysical assessment and comparison to ozonesondes, GOME-2B and OMI. *Atmospheric Measurement Techniques*, *14*(12), 7405–7433. https://doi.org/10.5194/amt-14-7405-2021

Ialongo, I., Herman, J., Krotkov, N., Lamsal, L., Boersma, K. F., Hovila, J., & Tamminen, J. (2016). Comparison of OMI NO_2 observations and their seasonal and weekly cycles with ground-based measurements in Helsinki. *Atmospheric Measurement Techniques*, *9*(10), 5203–5212. https://doi.org/10.5194/amt-9-5203-2016

Irie, H., Hoque, H. M. S., Damiani, A., Okamoto, H., Fatmi, A. M., Khatri, P., et al. (2019). Simultaneous observations by sky radiometer and MAX-DOAS for characterization of biomass burning plumes in central Thailand in January–April 2016. *Atmospheric Measurement Techniques*, *12*(1), 599–606. https://doi.org/10.5194/amt-12-599-2019

Irie, H., Takashima, H., Kanaya, Y., Boersma, K. F., Gast, L., Wittrock, F., et al. (2011). Eight-component retrievals from ground-based MAX-DOAS observations. *Atmospheric Measurement Techniques*, *4*(6), 1027–1044. https://doi.org/10.5194/amt-4-1027-2011

Javed, Z., Tanvir, A., Bilal, M., Su, W., Xia, C., Rehman, A., et al. (2021). Recommendations for HCHO and SO_2 retrieval settings from MAX-DOAS observations under different meteorological conditions. *Remote Sensing*, *13*(12), 2244. https://doi.org/10.3390/rs13122244

Javed, Z., Wang, Y., Xie, M., Tanvir, A., Rehman, A., Ji, X., et al. (2020). Investigating the impacts of the COVID-19 lockdown on trace gases using ground-based MAX-DOAS observations in Nanjing, China. *Remote Sensing*, *12*(23), 3939. https://doi.org/10.3390/rs12233939

Jin, J., Ma, J., Lin, W., Zhao, H., Shaiganfar, R., Beirle, S., & Wagner, T. (2016). MAX-DOAS measurements and satellite validation of tropospheric NO_2 and SO_2 vertical column densities at a rural site of North China. *Atmospheric Environment*, *133*, 12–25. https://doi.org/10.1016/j.atmosenv.2016.03.031

Johnson, M. S., Souri, A. H., Philip, S., Kumar, R., Naeger, A., Geddes, J., et al. (2023). Satellite remote-sensing capability to assess tropospheric-column ratios of formaldehyde and nitrogen dioxide: Case study during the long Island sound tropospheric ozone study 2018 (LISTOS 2018) field campaign. *Atmospheric Measurement Techniques*, *16*(9), 2431–2454. https://doi.org/10.5194/amt-16-2431-2023

KNMI. (2011). Regional tropospheric NO_2 columns from TROPOMI. Retrieved from https://www.temis.nl/airpollution/no2col/no2regio_tropomi.php

Krotkov, N. A., Lamsal, L. N., Celarier, E. A., Swartz, W. H., Marchenko, S. V., Bucsela, E. J., et al. (2017). The version 3 OMI NO_2 standard product. *Atmospheric Measurement Techniques*, *10*(9), 3133–3149. https://doi.org/10.5194/amt-10-3133-2017

Krotkov, N. A., Lamsal, L. N., Marchenko, S. V., Bucsela, E. J., Swartz, W. H., Joiner, J., & Team, T. O. C. (2019a). OMI/Aura nitrogen dioxide (NO2) total and tropospheric column 1-orbit L2 Swath 13 × 24 km V003 goddard earth sciences data and information services center (GES DISC). https://doi.org/10.5067/Aura/OMI/DATA2017

Krotkov, N. A., Lamsal, L. N., Marchenko, S. V., & Swartz, W. H. (2019b). OMNO2 README document data product version 4.0 9.0. Retrieved from https://aura.gesdisc.eosdis.nasa.gov/data/Aura_OMI_Level2/OMNO2.003/doc/README.OMNO2.pdf

Krotkov, N. A., McLinden, C. A., Li, C., Lamsal, L. N., Celarier, E. A., Marchenko, S. V., et al. (2016). Aura OMI observations of regional SO_2 and NO_2 pollution changes from 2005 to 2015. *Atmospheric Chemistry and Physics*, *16*(7), 4605–4629. https://doi.org/10.5194/acp-16-4605-2016

Lamsal, L. N., Krotkov, N. A., Celarier, E. A., Swartz, W. H., Pickering, K. E., Bucsela, E. J., et al. (2014). Evaluation of OMI operational standard NO_2 column retrievals using in situ and surface-based NO_2 observations. *Atmospheric Chemistry and Physics*, *14*(21), 11587–11609. https://doi.org/10.5194/acp-14-11587-2014

Lamsal, L. N., Krotkov, N. A., Vasilkov, A., Marchenko, S., Qin, W., Yang, E. S., et al. (2021). Ozone Monitoring Instrument (OMI) Aura nitrogen dioxide standard product version 4.0 with improved surface and cloud treatments. *Atmospheric Measurement Techniques*, *14*(1), 455–479. https://doi.org/10.5194/amt-14-455-2021

Lamsal, L. N., Martin, R. V., van Donkelaar, A., Celarier, E. A., Bucsela, E. J., Boersma, K. F., et al. (2010). Indirect validation of tropospheric nitrogen dioxide retrieved from the OMI satellite instrument: Insight into the seasonal variation of nitrogen oxides at northern midlatitudes. *Journal of Geophysical Research*, *115*(D5), D05302. https://doi.org/10.1029/2009JD013351

Laughner, J. L., Zare, A., & Cohen, R. C. (2016). Effects of daily meteorology on the interpretation of space-based remote sensing of NO_2. *Atmospheric Chemistry and Physics*, *16*(23), 15247–15264. https://doi.org/10.5194/acp-16-15247-2016

Lee, Y., Huey, L. G., Wang, Y., Qu, H., Zhang, R., Ji, Y., et al. (2021). Photochemistry of volatile organic compounds in the Yellow River Delta, China: Formation of O_3 and Peroxyacyl Nitrates. *Journal of Geophysical Research: Atmospheres*, *126*(23), e2021JD035296. https://doi.org/10.1029/2021JD035296

Leitão, J., Richter, A., Vrekoussis, M., Kokhanovsky, A., Zhang, Q. J., Beekmann, M., & Burrows, J. P. (2010). On the improvement of NO_2 satellite retrievals—Aerosol impact on the airmass factors. *Atmospheric Measurement Techniques*, *3*(2), 475–493. https://doi.org/10.5194/amt-3-475-2010

Levelt, P. F., Hilsenrath, E., Leppelmeier, G. W., Oord, G. H. J. V. D., Bhartia, P. K., Tamminen, J., et al. (2006). Science objectives of the ozone monitoring instrument. *IEEE Transactions on Geoscience and Remote Sensing*, *44*(5), 1199–1208. https://doi.org/10.1109/TGRS.2006.872336

Levelt, P. F., Joiner, J., Tamminen, J., Veefkind, J. P., Bhartia, P. K., Stein Zweers, D. C., et al. (2018). The ozone monitoring instrument: Overview of 14 years in space. *Atmospheric Chemistry and Physics*, *18*(8), 5699–5745. https://doi.org/10.5194/acp-18-5699-2018

Levy, J. I., Carrothers, T. J., Tuomisto, J. T., Hammitt, J. K., & Evans, J. S. (2001). Assessing the public health benefits of reduced ozone concentrations. *Environmental Health Perspectives*, *109*(12), 1215–1226. https://doi.org/10.1289/ehp.011091215

Li, D., Wang, S., Xue, R., Zhu, J., Zhang, S., Sun, Z., & Zhou, B. (2021). OMI-observed HCHO in Shanghai, China, during 2010–2019 and ozone sensitivity inferred by an improved HCHO / NO_2 ratio. *Atmospheric Chemistry and Physics*, *21*(20), 15447–15460. https://doi.org/10.5194/acp-21-15447-2021

Li, J., & Wang, Y. (2019). Inferring the anthropogenic NO_x emission trend over the United States during 2003–2017 from satellite observations: Was there a flattening of the emission trend after the great recession? *Atmospheric Chemistry and Physics*, *19*(24), 15339–15352. https://doi.org/10.5194/acp-19-15339-2019

Li, J., Wang, Y., Zhang, R., Smeltzer, C., Weinheimer, A., Herman, J., et al. (2021). Comprehensive evaluations of diurnal NO_2 measurements during DISCOVER-AQ 2011: Effects of resolution-dependent representation of NO_x emissions. *Atmospheric Chemistry and Physics*, *21*(14), 11133–11160. https://doi.org/10.5194/acp-21-11133-2021

Li, K., Jacob, D. J., Shen, L., Lu, X., De Smedt, I., & Liao, H. (2020). Increases in surface ozone pollution in China from 2013 to 2019: Anthropogenic and meteorological influences. *Atmospheric Chemistry and Physics*, *20*(19), 11423–11433. https://doi.org/10.5194/acp-20-11423-2020

Lin, H., Xing, C., Hong, Q., Liu, C., Ji, X., Liu, T., et al. (2022). Diagnosis of ozone formation sensitivities in different height layers via MAX-DOAS observations in Guangzhou. *Journal of Geophysical Research: Atmospheres*, *127*(15), e2022JD036803. https://doi.org/10.1029/2022JD036803

Lin, J. T., Martin, R. V., Boersma, K. F., Sneep, M., Stammes, P., Spurr, R., et al. (2014). Retrieving tropospheric nitrogen dioxide from the ozone monitoring instrument: Effects of aerosols, surface reflectance anisotropy, and vertical profile of nitrogen dioxide. *Atmospheric Chemistry and Physics*, *14*(3), 1441–1461. https://doi.org/10.5194/acp-14-1441-2014

Lippmann, M. (1989). Health effects of ozone a critical review. *JAPCA*, *39*(5), 672–695. https://doi.org/10.1080/08940630.1989.10466554

Liu, C., Gao, M., Hu, Q., Brasseur, G. P., & Carmichael, G. R. (2021). Stereoscopic monitoring: A promising strategy to advance diagnostic and prediction of air pollution. *Bulletin of the American Meteorological Society*, *102*(4), E730–E737. https://doi.org/10.1175/BAMS-D-20-0217.1

Liu, X., Zhang, Y., Huey, L. G., Yokelson, R. J., Wang, Y., Jimenez, J. L., et al. (2016). Agricultural fires in the southeastern U.S. during SEAC4RS: Emissions of trace gases and particles and evolution of ozone, reactive nitrogen, and organic aerosol. *Journal of Geophysical Research: Atmospheres*, *121*(12), 7383–7414. https://doi.org/10.1002/2016JD025040

Liu, Z., Wang, Y., Costabile, F., Amoroso, A., Zhao, C., Huey, L. G., et al. (2014). Evidence of aerosols as a media for rapid daytime HONO production over China. *Environmental Science & Technology*, *48*(24), 14386–14391. https://doi.org/10.1021/es504163z

Liu, Z., Wang, Y., Gu, D., Zhao, C., Huey, L. G., Stickel, R., et al. (2012). Summertime photochemistry during CAREBeijing-2007: RO_x budgets and O_3 formation. *Atmospheric Chemistry and Physics*, *12*(16), 7737–7752. https://doi.org/10.5194/acp-12-7737-2012

Logan, J. A. (1983). Nitrogen oxides in the troposphere: Global and regional budgets. *Journal of Geophysical Research*, *88*(C15), 10785–10807. https://doi.org/10.1029/JC088iC15p10785

Lorente, A., Boersma, K. F., Stammes, P., Tilstra, L. G., Richter, A., Yu, H., et al. (2018). The importance of surface reflectance anisotropy for cloud and NO_2 retrievals from GOME-2 and OMI. *Atmospheric Measurement Techniques*, *11*(7), 4509–4529. https://doi.org/10.5194/amt-11-4509-2018

Lorente, A., Folkert Boersma, K., Yu, H., Dörner, S., Hilboll, A., Richter, A., et al. (2017). Structural uncertainty in air mass factor calculation for NO_2 and HCHO satellite retrievals. *Atmospheric Measurement Techniques*, *10*(3), 759–782. https://doi.org/10.5194/amt-10-759-2017

Ma, J. Z., Beirle, S., Jin, J. L., Shaiganfar, R., Yan, P., & Wagner, T. (2013). Tropospheric NO_2 vertical column densities over Beijing: Results of the first three years of ground-based MAX-DOAS measurements (2008–2011) and satellite validation. *Atmospheric Chemistry and Physics*, *13*(3), 1547–1567. https://doi.org/10.5194/acp-13-1547-2013

McColl, K. A., Vogelzang, J., Konings, A. G., Entekhabi, D., Piles, M., & Stoffelen, A. (2014). Extended triple collocation: Estimating errors and correlation coefficients with respect to an unknown target. *Geophysical Research Letters*, *41*(17), 6229–6236. https://doi.org/10.1002/2014GL061322

Nuvolone, D., Petri, D., & Voller, F. (2018). The effects of ozone on human health. *Environmental Science and Pollution Research*, *25*(9), 8074–8088. https://doi.org/10.1007/s11356-017-9239-3

Palmer, P. I., Jacob, D. J., Chance, K., Martin, R. V., Spurr, R. J. D., Kurosu, T. P., et al. (2001). Air mass factor formulation for spectroscopic measurements from satellites: Application to formaldehyde retrievals from the Global Ozone Monitoring Experiment. *Journal of Geophysical Research*, *106*(D13), 14539–14550. https://doi.org/10.1029/2000JD900772

Peng, Q., Palm, B. B., Fredrickson, C. D., Lee, B. H., Hall, S. R., Ullmann, K., et al. (2022). Direct constraints on secondary HONO production in aged wildfire smoke from airborne measurements over the Western US. *Geophysical Research Letters*, *49*(15), e2022GL098704. https://doi.org/10.1029/2022GL098704

Platt, U., & Stutz, J. (2008). Differential oprical absorption spectroscopy. In *Physics of Earth and space Environments*. Springer. https://doi.org/10.1007/978-3-540-75776-4

Pu, D., Zhu, L., De Smedt, I., Li, X., Sun, W., Wang, D., et al. (2022). Response of anthropogenic volatile organic compound emissions to urbanization in Asia probed with TROPOMI and VIIRS satellite observations. *Geophysical Research Letters*, *49*(18), e2022GL099470. https://doi.org/10.1029/2022GL099470

Qin, W., Fasnacht, Z., Haffner, D., Vasilkov, A., Joiner, J., Krotkov, N., et al. (2019). A geometry-dependent surface Lambertian-equivalent reflectivity product for UV–Vis retrievals—Part 1: Evaluation over land surfaces using measurements from OMI at 466 nm. *Atmospheric Measurement Techniques*, *12*(7), 3997–4017. https://doi.org/10.5194/amt-12-3997-2019

Qu, H., Wang, Y., Zhang, R., & Li, J. (2020). Extending ozone-precursor relationships in China from peak concentration to peak time. *Journal of Geophysical Research: Atmospheres*, *125*(22), e2020JD033670. https://doi.org/10.1029/2020JD033670

Qu, H., Wang, Y., Zhang, R., Liu, X., Huey, L. G., Sjostedt, S., et al. (2021). Chemical production of oxygenated volatile organic compounds strongly enhances boundary-layer oxidation chemistry and ozone production. *Environmental Science & Technology*, *55*(20), 13718–13727. https://doi.org/10.1021/acs.est.1c04489

Riess, T. C. V. W., Boersma, K. F., van Vliet, J., Peters, W., Sneep, M., Eskes, H., & van Geffen, J. (2022). Improved monitoring of shipping NO_2 with TROPOMI: Decreasing NO_x emissions in European seas during the COVID-19 pandemic. *Atmospheric Measurement Techniques*, *15*(5), 1415–1438. https://doi.org/10.5194/amt-15-1415-2022

Roberts, J. M., Stockwell, C. E., Yokelson, R. J., de Gouw, J., Liu, Y., Selimovic, V., et al. (2020). The nitrogen budget of laboratory-simulated western US wildfires during the FIREX 2016 Fire Lab study. *Atmospheric Chemistry and Physics*, *20*(14), 8807–8826. https://doi.org/10.5194/acp-20-8807-2020

Rodgers, C. D. (2000). Inverse methods for atmospheric sounding. https://doi.org/10.1142/3171

Sekiya, T., Miyazaki, K., Eskes, H., Sudo, K., Takigawa, M., & Kanaya, Y. (2022). A comparison of the impact of TROPOMI and OMI tropospheric NO_2 on global chemical data assimilation. *Atmospheric Measurement Techniques*, *15*(6), 1703–1728. https://doi.org/10.5194/amt-15-1703-2022

Shaiganfar, R., Beirle, S., Petetin, H., Zhang, Q., Beekmann, M., & Wagner, T. (2015). New concepts for the comparison of tropospheric NO_2 column densities derived from car-MAX-DOAS observations, OMI satellite observations and the regional model CHIMERE during two MEGAPOLI campaigns in Paris 2009/10. *Atmospheric Measurement Techniques*, *8*(7), 2827–2852. https://doi.org/10.5194/amt-8-2827-2015

Shim, C., Wang, Y., Choi, Y., Palmer, P. I., Abbot, D. S., & Chance, K. (2005). Constraining global isoprene emissions with Global Ozone Monitoring Experiment (GOME) formaldehyde column measurements. *Journal of Geophysical Research*, *110*(D24), D24301. https://doi.org/10.1029/2004jd005629

Smedt, I. D., Geffen, J. V., Richter, A., Beirle, S., Yu, H., Vlietinck, J., et al. (2017). Product user guide for HCHO 1.0. Retrieved from https://www.temis.nl/qa4ecv/hcho/QA4ECV_HCHO_PSD_v1.0.pdf

Song, Y., Xing, C., Liu, C., Lin, J., Wu, H., Liu, T., et al. (2023). Evaluation of transport processes over North China plain and Yangtze river Delta using MAX-DOAS observations. *Atmospheric Chemistry and Physics*, *23*(3), 1803–1824. https://doi.org/10.5194/acp-23-1803-2023

Souri, A. H., Johnson, M. S., Wolfe, G. M., Crawford, J. H., Fried, A., Wisthaler, A., et al. (2022). Characterization of errors in satellite-based HCHO/NO_2 tropospheric column ratios with respect to chemistry, column to PBL translation, spatial representation, and retrieval uncertainties. *Atmospheric Chemistry and Physics Discussions*, *2022*, 1–43. https://doi.org/10.5194/acp-2022-410

Stavrakou, T., Müller, J. F., Bauwens, M., Boersma, K. F., & van Geffen, J. (2020). Satellite evidence for changes in the NO_2 weekly cycle over large cities. *Scientific Reports*, *10*(1), 10066. https://doi.org/10.1038/s41598-020-66891-0

Stoffelen, A. (1998). Toward the true near-surface wind speed: Error modeling and calibration using triple collocation. *Journal of Geophysical Research*, *103*(C4), 7755–7766. https://doi.org/10.1029/97JC03180

Su, W., Liu, C., Chan, K. L., Hu, Q., Liu, H., Ji, X., et al. (2020). An improved TROPOMI tropospheric HCHO retrieval over China. *Atmospheric Measurement Techniques*, *13*(11), 6271–6292. https://doi.org/10.5194/amt-13-6271-2020

Theys, N., Volkamer, R., Müller, J. F., Zarzana, K. J., Kille, N., Clarisse, L., et al. (2020). Global nitrous acid emissions and levels of regional oxidants enhanced by wildfires. *Nature Geoscience*, *13*(10), 681–686. https://doi.org/10.1038/s41561-020-0637-7

Urbanski, S. P. (2013). Combustion efficiency and emission factors for wildfire-season fires in mixed conifer forests of the northern Rocky Mountains, US. *Atmospheric Chemistry and Physics*, *13*(14), 7241–7262. https://doi.org/10.5194/acp-13-7241-2013

van Geffen, J., Eskes, H., Boersma, K. F., & Veefkind, J. P. (2021). TROPOMI ATBD of the total and tropospheric NO_2 data products 2.2.0. Retrieved from http://www.tropomi.eu/data-products/nitrogen-dioxide/

van Geffen, J., Eskes, H., Compernolle, S., Pinardi, G., Verhoelst, T., Lambert, J. C., et al. (2022). Sentinel-5P TROPOMI NO_2 retrieval: Impact of version v2.2 improvements and comparisons with OMI and ground-based data. *Atmospheric Measurement Techniques*, *15*(7), 2037–2060. https://doi.org/10.5194/amt-15-2037-2022

Vasilkov, A., Qin, W., Krotkov, N., Lamsal, L., Spurr, R., Haffner, D., et al. (2017). Accounting for the effects of surface BRDF on satellite cloud and trace-gas retrievals: A new approach based on geometry-dependent Lambertian equivalent reflectivity applied to OMI algorithms. *Atmospheric Measurement Techniques*, *10*(1), 333–349. https://doi.org/10.5194/amt-10-333-2017

Vasilkov, A., Yang, E. S., Marchenko, S., Qin, W., Lamsal, L., Joiner, J., et al. (2018). A cloud algorithm based on the O2-O2 477 nm absorption band featuring an advanced spectral fitting method and the use of surface geometry-dependent Lambertian-equivalent reflectivity. *Atmospheric Measurement Techniques*, *11*(7), 4093–4107. https://doi.org/10.5194/amt-11-4093-2018

Veefkind, J. P., Aben, I., McMullan, K., Förster, H., de Vries, J., Otter, G., et al. (2012). TROPOMI on the ESA Sentinel-5 precursor: A GMES mission for global observations of the atmospheric composition for climate, air quality and ozone layer applications. *Remote Sensing of Environment*, *120*, 70–83. https://doi.org/10.1016/j.rse.2011.09.027

Verhoelst, T., Compernolle, S., Pinardi, G., Lambert, J. C., Eskes, H. J., Eichmann, K. U., et al. (2021). Ground-based validation of the Copernicus Sentinel-5P TROPOMI NO_2 measurements with the NDACC ZSL-DOAS, MAX-DOAS and Pandonia global networks. *Atmospheric Measurement Techniques*, *14*(1), 481–510. https://doi.org/10.5194/amt-14-481-2021

Wang, H. J. R., Damadeo, R., Flittner, D., Kramarova, N., Taha, G., Davis, S., et al. (2020). Validation of SAGE III/ISS solar occultation ozone products with correlative satellite and ground-based measurements. *Journal of Geophysical Research: Atmospheres*, *125*(11), e2020JD032430. https://doi.org/10.1029/2020JD032430

Wang, P., Holloway, T., Bindl, M., Harkey, M., & De Smedt, I. (2022). Ambient formaldehyde over the United States from ground-based (AQS) and satellite (OMI) observations. *Remote Sensing*, *14*(9), 2191. https://doi.org/10.3390/rs14092191

Wang, P., Stammes, P., van der A, R., Pinardi, G., & van Roozendael, M. (2008). FRESCO+: An improved O_2 A-band cloud retrieval algorithm for tropospheric trace gas retrievals. *Atmospheric Chemistry and Physics*, *8*(21), 6565–6576. https://doi.org/10.5194/acp-8-6565-2008

Wang, Y., Apituley, A., Bais, A., Beirle, S., Benavent, N., Borovski, A., et al. (2020). Inter-comparison of MAX-DOAS measurements of tropospheric HONO slant column densities and vertical profiles during the CINDI-2 campaign. *Atmospheric Measurement Techniques*, *13*(9), 5087–5116. https://doi.org/10.5194/amt-13-5087-2020

Wang, Y., Beirle, S., Lampel, J., Koukouli, M., De Smedt, I., Theys, N., et al. (2017). Validation of OMI, GOME-2A and GOME-2B tropospheric NO_2, SO_2 and HCHO products using MAX-DOAS observations from 2011 to 2014 in Wuxi, China: Investigation of the effects of priori profiles and aerosols on the satellite products. *Atmospheric Chemistry and Physics*, *17*(8), 5007–5033. https://doi.org/10.5194/acp-17-5007-2017

Wang, Y., Dörner, S., Donner, S., Böhnke, S., De Smedt, I., Dickerson, R. R., et al. (2019). Vertical profiles of NO_2, SO_2, HONO, HCHO, CHOCHO and aerosols derived from MAX-DOAS measurements at a rural site in the central western North China Plain and their relation to emission sources and effects of regional transport. *Atmospheric Chemistry and Physics*, *19*(8), 5417–5449. https://doi.org/10.5194/acp-19-5417-2019

Wang, Y., Jacob, D. J., & Logan, J. A. (1998). Global simulation of tropospheric O3-NOx-hydrocarbon chemistry: 1. Model formulation.

Wang, Y., Lampel, J., Xie, P., Beirle, S., Li, A., Wu, D., & Wagner, T. (2017). Ground-based MAX-DOAS observations of tropospheric aerosols, NO_2, SO_2 and HCHO in Wuxi, China, from 2011 to 2014. *Atmospheric Chemistry and Physics*, *17*(3), 2189–2215. https://doi.org/10.5194/acp-17-2189-2017

Wang, Y., Puķīte, J., Wagner, T., Donner, S., Beirle, S., Hilboll, A., et al. (2018). Vertical profiles of tropospheric ozone from MAX-DOAS measurements during the CINDI-2 campaign: Part 1—Development of a new retrieval algorithm. *Journal of Geophysical Research: Atmospheres*, *123*(18), 10637–610670. https://doi.org/10.1029/2018JD028647

Williams, J. E., Boersma, K. F., Le Sager, P., & Verstraeten, W. W. (2017). The high-resolution version of TM5-MP for optimized satellite retrievals: Description and validation. *Geoscientific Model Development*, *10*(2), 721–750. https://doi.org/10.5194/gmd-10-721-2017

Xia, C., Liu, C., Cai, Z., Duan, X., Hu, Q., Zhao, F., et al. (2021). Improved anthropogenic SO_2 retrieval from high-spatial-resolution satellite and its application during the COVID-19 pandemic. *Environmental Science & Technology*, *55*(17), 11538–11548. https://doi.org/10.1021/acs.est.1c01970

Xing, C., Liu, C., Wang, S., Chan, K. L., Gao, Y., Huang, X., et al. (2017). Observations of the vertical distributions of summertime atmospheric pollutants and the corresponding ozone production in Shanghai, China. *Atmospheric Chemistry and Physics*, *17*(23), 14275–14289. https://doi.org/10.5194/acp-17-14275-2017

Xu, W. Y., Zhao, C. S., Ran, L., Deng, Z. Z., Liu, P. F., Ma, N., et al. (2011). Characteristics of pollutants and their correlation to meteorological conditions at a suburban site in the North China Plain. *Atmospheric Chemistry and Physics*, *11*(9), 4353–4369. https://doi.org/10.5194/acp-11-4353-2011

Ye, C., Zhou, X., Pu, D., Stutz, J., Festa, J., Spolaor, M., et al. (2016). Rapid cycling of reactive nitrogen in the marine boundary layer. *Nature*, *532*(7600), 489–491. https://doi.org/10.1038/nature17195

Zara, M., Boersma, K. F., De Smedt, I., Richter, A., Peters, E., van Geffen, J. H. G. M., et al. (2018). Improved slant column density retrieval of nitrogen dioxide and formaldehyde for OMI and GOME-2A from QA4ECV: Intercomparison, uncertainty characterisation, and trends. *Atmospheric Measurement Techniques*, *11*(7), 4033–4058. https://doi.org/10.5194/amt-11-4033-2018

Zeng, T., Wang, Y., Yoshida, Y., Tian, D., Russell, A. G., & Barnard, W. R. (2008). Impacts of prescribed fires on air quality over the Southeastern United States in spring based on modeling and ground/satellite measurements. *Environmental Science & Technology*, *42*(22), 8401–8406. https://doi.org/10.1021/es800363d

Zhang, C., Liu, C., Chan, K. L., Hu, Q., Liu, H., Li, B., et al. (2020). First observation of tropospheric nitrogen dioxide from the environmental trace gases monitoring instrument onboard the GaoFen-5 satellite. *Light: Science and Applications*, *9*(1), 66. https://doi.org/10.1038/s41377-020-0306-z

Zhang, R., Wang, Y., Smeltzer, C., Qu, H., Koshak, W., & Boersma, K. F. (2018). Comparing OMI-based and EPA AQS in situ NO_2 trends: Towards understanding surface NOx emission changes. *Atmospheric Measurement Techniques*, *11*(7), 3955–3967. https://doi.org/10.5194/amt-11-3955-2018

Zhang, R., Zhang, Y., Lin, H., Feng, X., Fu, T.-M., & Wang, Y. (2020). NOx emission reduction and recovery during COVID-19 in east China. *Atmosphere*, *11*(4), 433. https://doi.org/10.3390/atmos11040433

Zhang, Y., Wang, Y., Crawford, J., Cheng, Y., & Li, J. (2018). Improve observation-based ground-level ozone spatial distribution by compositing satellite and surface observations: A simulation experiment. *Atmospheric Environment*, *180*, 226–233. https://doi.org/10.1016/j.atmosenv.2018.02.044

Zhao, C., & Wang, Y. (2009). Assimilated inversion of NO_x emissions over East Asia using OMI NO_2 column measurements. *Geophysical Research Letters*, *36*(6), L06805. https://doi.org/10.1029/2008GL037123

Zheng, X., Javed, Z., Liu, C., Tanvir, A., Sandhu, O., Liu, H., et al. (2022). MAX-DOAS and In-situ measurements of aerosols and trace gases over Dongying, China: Insight into Ozone formation sensitivity based on Secondary HCHO. *Journal of Environmental Sciences*, *135*, 656–668. https://doi.org/10.1016/j.jes.2022.09.014

Zwieback, S., Scipal, K., Dorigo, W., & Wagner, W. (2012). Structural and statistical properties of the collocation technique for error characterization. *Nonlinear Processes in Geophysics*, *19*(1), 69–80. https://doi.org/10.5194/npg-19-69-2012